BIROn - Birkbeck Institutional Research Online

Multiple sites of recent wet-based glaciation identified from eskers in western Tempe Terra, Mars

Savana Z. Woodley [a],[*],[1], Frances E.G. Butcher [a], Peter Fawdon [b], Chris D. Clark [a], Felix S.L. Ng [a], Joel M. Davis [c], Colman Gallagher [d],[e]

[a] *Department of Geography, The University of Sheffield, Sheffield S10 2TN, UK*
[b] *School of Physical Sciences, The Open University, Milton Keynes MK7 6AA, UK*
[c] *Department of Earth Sciences, Natural History Museum, London SW7 5BD, UK*
[d] *UCD School of Geography, University College Dublin, Dublin, Ireland*
[e] *UCD Earth Institute, University College Dublin, Dublin, Ireland*

A B S T R A C T

Precipitation in Mars' mid-latitudes formed Viscous Flow Features (VFFs), landforms analogous to terrestrial debris-covered glaciers, in the last 1 Gyr. Until recently, the prevailing view was that the Amazonian environment was not conducive to basal melting of VFFs. However, recent identification of VFF-linked eskers (sedimentary ridges deposited by meltwater in sub-glacial tunnels) in Phlegra Montes and Tempe Terra suggests localized basal melting has occurred. We identify two VFF-linked sinuous ridges in western Tempe Terra, which we propose are two additional eskers. To explore this hypothesis, we produce a 1:300,000 map of the geomorphology of western Tempe Terra, use impact crater counts to constrain the age of the sinuous ridges, and analyze the morphology and morphometry of the sinuous ridges. Mapping reveals a heavily deformed Noachian massif that was embayed by younger volcanic material and subsequently glaciated. The sinuous ridges lie 3–7 km from the VFF-termini and are associated with mounds which we interpret as ice-cored moraines. After considering multiple formation hypotheses (including inverted paleochannels and volcanic features) and comparing morphometries to Martian and terrestrial eskers, we suggest that both the sinuous ridges are of glacial origin and most likely eskers. This shows that basal melting of VFFs occurred at more than one location in Tempe Terra, at least transiently. Thus, our identification of two additional candidate eskers in Tempe Terra suggests that the late Amazonian thermal environment may have been more complex than previously thought and contributes to a better characterization of the recent glacial history of the region.

1. Introduction

The Martian cryosphere is perhaps the most characteristic feature of the Amazonian epoch. Liquid water, available from the Noachian and Hesperian epochs (Carr and Head, 2010; Malin and Edgett, 2003), was sequestered into a global cryosphere throughout the Amazonian (e.g., Squyres et al., 1992). Currently, water-ice is contained in the polar ice caps and in the mid-latitudes as ground-ice, ice-containing mantling deposits, and viscous flow features (e.g., Head et al., 2003; Lasue et al., 2013; Levy et al., 2010a; Schon et al., 2009). Viscous Flow Features (VFFs) are considered to be most analogous to debris-covered glaciers

(Head et al., 2010; Holt et al., 2008; Levy et al., 2010b) that are relics of Amazonian orbital conditions permitting mid-latitude precipitation and ice accumulation (Laskar et al., 2004). However, during much of the Amazonian, the climate has been cold and hyper-arid, with low atmospheric pressures causing water to be unstable at Mars' surface. In general, VFFs are thought to have been persistently cold-based since their formation.

However, recent identifications of VFF-linked eskers in Phlegra Montes (Gallagher and Balme, 2015), northwest Tempe Terra (Butcher et al., 2017, 2020), and possibly in Chukhung crater in central Tempe Terra (Butcher et al., 2021), suggest that localized basal melting of VFF

could have occurred in some locations during the Amazonian. Eskers are sedimentary ridges that are deposited by meltwater in subglacial tunnels (e.g., Shreve, 1985). Their identification in association with VFFs suggests that glacial meltwater has been produced by localized basal melting of those VFFs in the last 100s of Ma (Butcher et al., 2017, 2020, 2021; Gallagher and Balme, 2015). The apparent scarcity of VFF-linked eskers elsewhere in Mars' mid-latitudes suggests that meltwater production was not driven solely by climate-induced warming, but also by local factors such as elevated geothermal heat flux and strain heating (Butcher et al., 2017; Gallagher and Balme, 2015).

Recent additional evidence of a regional landscape of warm-based glacial erosion in Phlegra Montes (Gallagher et al., 2021), within which one of the VFF-linked eskers is located (Gallagher and Balme, 2015), suggests that more regional-scale climatic change could have been required, and that we do not have a complete picture of environmental change on Amazonian Mars. Further identification of VFF-linked eskers, if present, would contribute to our understanding of Mars' glacial history, and of past variations in the surface/near-surface thermal environment.

We identify two sinuous ridges in association with VFFs in western Tempe Terra (Fig. 1), only ~150 km S-SW of a similar sinuous ridge that is interpreted as a VFF-linked esker in northwest Tempe Terra (Butcher et al., 2017). We present a geomorphic map of western Tempe Terra, constrain the formation age of the two newly-identified sinuous ridges, and conduct a morphometric analysis of the sinuous ridges. Our study provides additional context into the glacial history of Tempe Terra and provides morphometrics of candidate eskers that can be used to aid in the characterization and identification of similar features across Mars.

2. Study Area: Western Tempe Terra

Tempe Terra lies in Mars' northern mid-latitudes (30–50°N and 90–65°W), to the northeast of the Tharsis volcano-tectonic province (Fig. 1A). The region comprises a plateau of heavily cratered Noachian highland terrain, locally superposed by Hesperian volcanic plains and Amazonian aprons (Tanaka et al., 2014a, 2014b). There are many volcanic vents and small shield volcanoes in southwest Tempe Terra, which mostly formed in the last 1 Ga but with some as old as 2.3 Ga (Richardson et al., 2021). Tempe Terra has a complex tectonic history, with extensional deformation occurring in three phases (Middle Noachian, Early Hesperian, and Early Amazonian; Bouley et al., 2018). The large unnamed tectonic graben system in western Tempe Terra formed ~3.5–4.0 Ga (Hauber et al., 2010).

Our study area is a 23,000 km² region in western Tempe Terra (Fig. 1B). Of particular interest are two sinuous ridge systems that emerge from Amazonian-aged glacial deposits (e.g., Tanaka et al., 2014a, 2014b; Van Gasselt et al., 2011) and extend into a large graben (Fig. 1C). The sinuous ridges are broadly parallel and lie ~60 km apart; the northern sinuous ridge is referred to as System I (Fig. 1D), and the southern ridge as System II (Fig. 1E).

Sinuous ridges elsewhere in Tempe Terra have been interpreted as candidate eskers (Fig. 1B), including in an unnamed graben in northwest Tempe Terra, adjacent to our study area (Butcher et al., 2017, 2020). In Chukhung Crater, ~600 km southeast of our study area, sinuous ridges have been interpreted as eskers and/or pre-glacial fluvial features (Butcher et al., 2021).

3. Data and methods

3.1. Morphological mapping

We produced a 1:300,000 geomorphological map of our study area using a basemap we generated from mosaicked ~6 m/pixel Context Camera images (CTX; Malin et al., 2007; Fig. 1C). Where available, we used ~25 cm/pixel High Resolution Imaging Science Experiment (HiRISE; McEwen et al., 2007) images to scrutinize superposition

relationships and supplement mapping observations. To construct cross sections and provide stratigraphic context, we used a ~75 m/pixel High Resolution Stereo Camera (HRSC; Neukum et al., 2004) digital elevation model (DEM). We digitized the geomorphological map in *Environmental Systems Research Institute ArcGIS 10.7*, using a sinuosidal projection with the meridian line centered at 82.8°W between the two sinuous ridges to minimize cartographic distortion.

3.2. Sinuous ridge morphometry

We collected morphometry measurements of the two sinuous ridges, following methods by Storrar et al. (2014) and Butcher et al. (2016, 2020). This included 2D planform geometries (such as length and sinuosity) of both sinuous ridges, and 3D cross-sectional geometries (such as height and width) of System II only. We used these morphometries to consider formation mechanisms for the sinuous ridges and to compare them to similar features on Mars that have been interpreted as eskers (Butcher, 2019; Butcher et al., 2020) and to eskers on Earth (Storrar et al., 2013, 2014). To take the 3D measurements, we produced a DEM from stereo-pair HiRISE images ESP_061969_2240 and ESP_062048_2240, following methods by Kirk et al. (2008). Using *ISIS 3.0* and *SOCET SET 5.6.0*, we generated a 1 m/pixel HiRISE DEM and a corresponding 25 cm/pixel orthorectified image. We derived uncertainties, and found that the horizontal measurement uncertainty due to map projection is ±0.0001 m and the vertical HiRISE DEM precision is ±0.113 m (for further method uncertainties, see Supplementary Materials 1).

3.2.1. Measurement of 2D morphometries

We digitized the crests of sinuous ridge segments as polylines using HiRISE images, aided by aspect maps and contour lines from the HiRISE DEM and HRSC DEM. We define *segments* as unbroken ridge sections, and *systems* as sets of aligned sections which belong to the same ridge structure.

For each segment, we measured the segment length (L_s) and segment path length (P_s) and used these to calculate the segment sinuosity (S_s) as the ratio between L_s and P_s (Butcher, 2019). We defined L_s as the length of an unbroken ridge crest and P_s as the straight-line length from start-point to end-point of an individual segment (Butcher et al., 2016; Storrar et al., 2014).

For each system, we determined the mapped system length (L_m), the interpolated system length (L_i), and the system path length (P_i) and used these to calculate system sinuosity (S_i) and continuity (C) using Eqs. 5.3 and 5.1 from Butcher (2019). We defined L_m as the combined length of all individual segments, L_i as the mapped system length plus the linear distance between segments, and P_i as the straight-line length from start-point to end-point of the system (Butcher et al., 2016; Storrar et al., 2014). The calculated sinuosity is a measure of system or segment linearity, and the continuity is a measure of system fragmentation.

3.2.2. Measurement of 3D morphometries

We digitized ridge-perpendicular transects at 40 m intervals, excluding transects <40 m from a segment's start or end point or where the ridge showed clear modification (for example by impact craters). For each transect, we recorded the crest elevation (Z_{crest}), left and right base point elevation (Z_{left} and Z_{right}), and distance along the transect of each base point (W_{left} and W_{right}). We calculated ridge height (H), elevation of base (Z_{base}), ridge width (W), and width-height ratio (A) using Eqs. 5.4–5.7 from Butcher (2019).

3.3. Impact crater retention age

The size-frequency distribution of impact craters of the two sinuous ridges cannot be directly determined as the ridges have too small a surface area and too few impact craters. Instead, we determined the impact crater retention age of two geomorphological map units, one
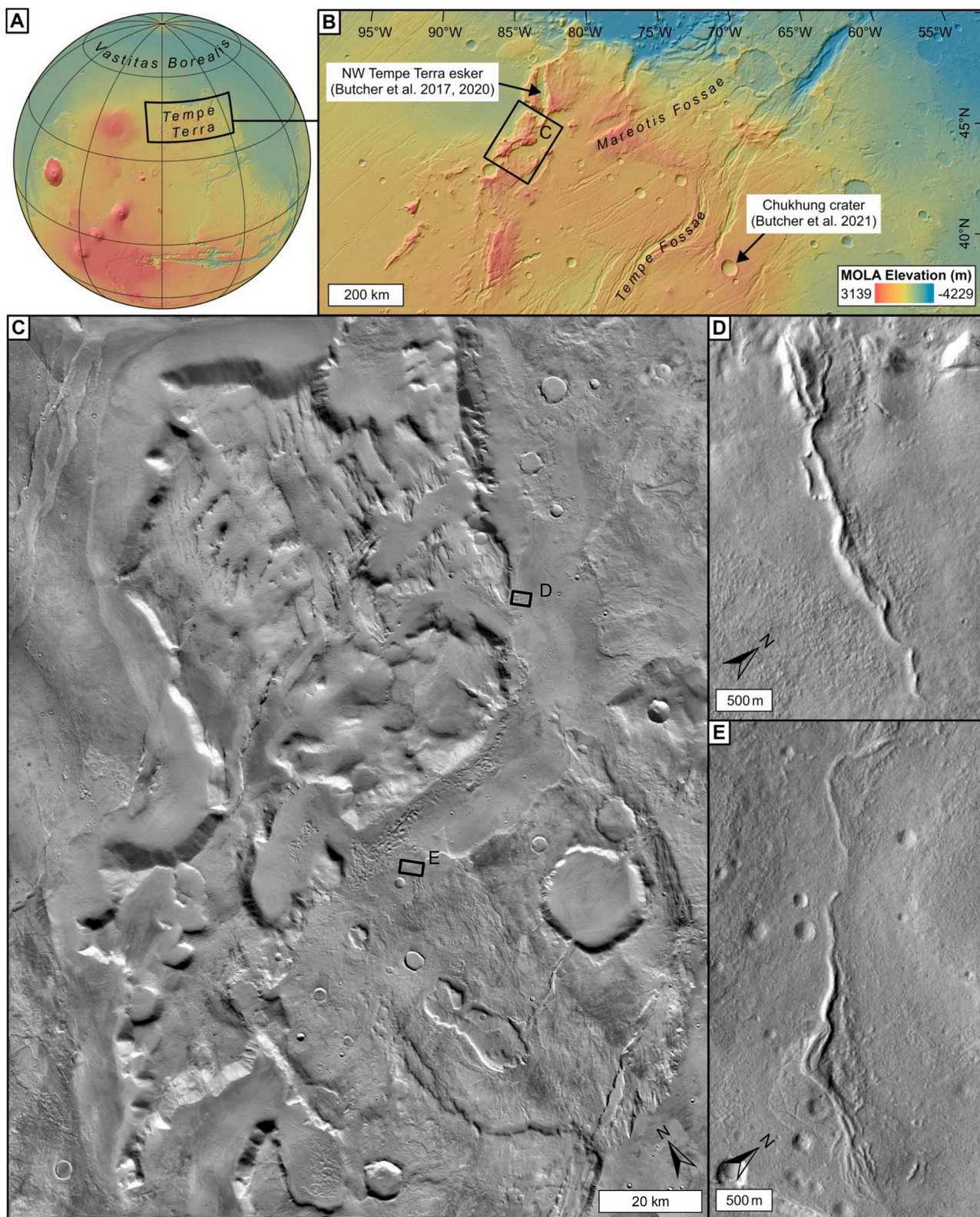
Fig. 1. The location of west Tempe Terra, Mars, and the two sinuous ridges. Black boxes show the location and extent of subsequent panels. Data types and product IDs are listed in Supplementary Materials 1. (A) Global topographic MOLA map. (B) Regional topographic MOLA map of Tempe Terra. (C) CTX image mosaic of the study area in western Tempe Terra. (D) Sinuous ridge System I in CTX, centered at 44.334°N, 83.295°W. (E) Sinuous ridge System II in CTX, centered at 43.772°N, 84.387°W.

which underlies the sinuous ridges and one which overlies them. This gives the relative formation age of the sinuous ridges and a time bracket in which they formed. The first count area lies within the *upper flow unit* (see Section 4.1) which underlies System I. As this unit is not homogenous and appears to comprise multiple layers of different ages, we selected the western part of this unit as the count area as it appears to comprise the uppermost layer based on a higher elevation and a less degraded appearance. The remaining two count areas lie within the

apron unit (see Section 4.1), from which both sinuous ridges extend.

We used the ArcGIS extension *CraterTools* (Kneissl et al., 2011) to measure impact crater diameters from CTX images. We used *CraterStats 2.0* (Michael and Neukum, 2010) to estimate the crater retention age, by applying the Ivanov (2001) production function and the Hartmann and Neukum (2001)chronology function. The resulting crater retention ages are best-fit estimates, but may have significant uncertainties, due to relatively small count areas, small sample sizes, and reliance on craters
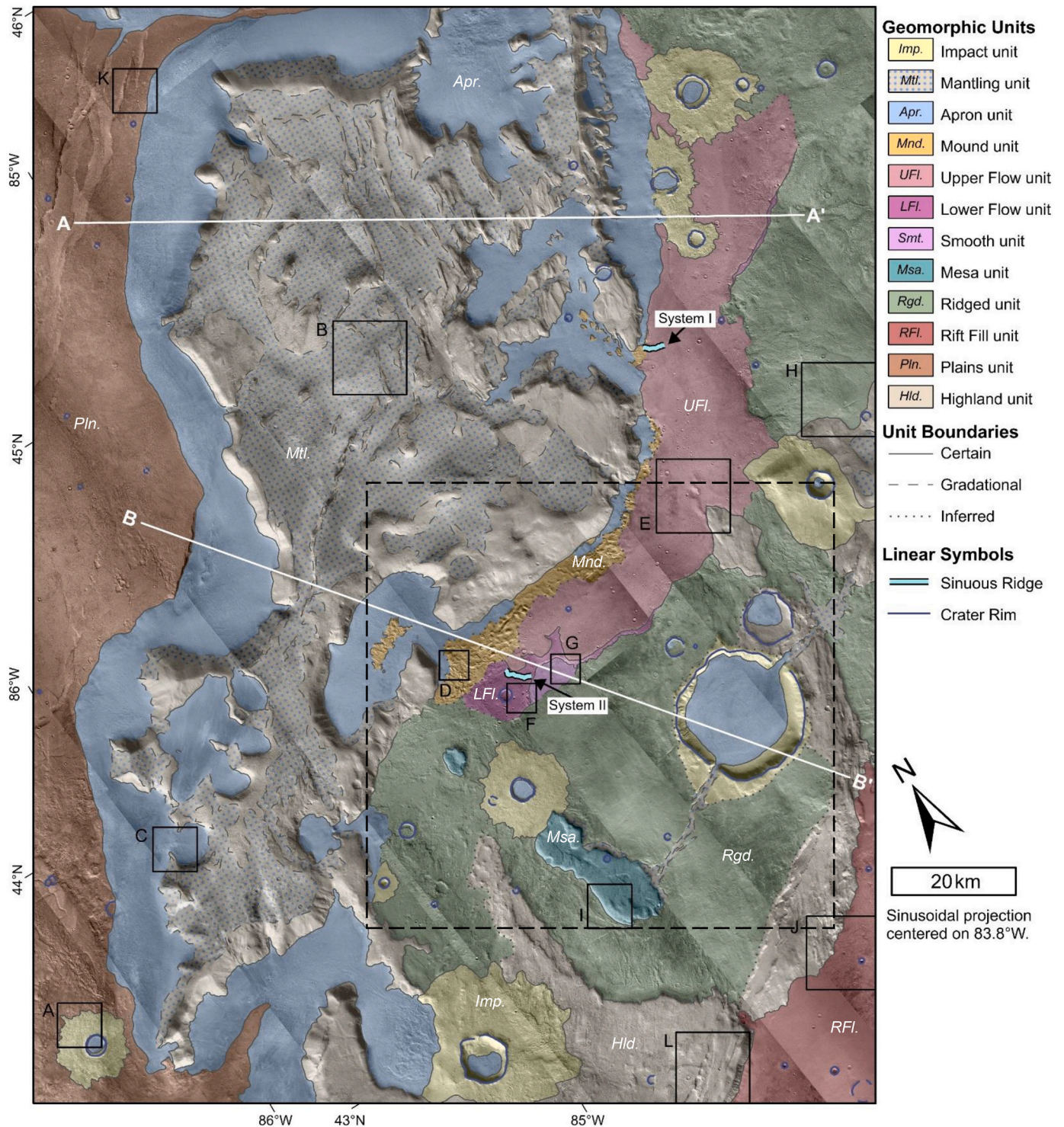

Fig. 2. Geomorphic map of west Tempe Terra, Mars. CTX basemap with solid black boxes showing the location and extent of panels in Fig. 3, white lines showing the location of cross sections A-A' and B-B′ in Fig. 4, and the black dashed box showing the location and extent of Fig. 5A. Data types and product IDs are listed in Supplementary Materials 1.

with small diameters (Hartmann, 2005; Warner et al., 2015).

4. Observations and results

4.1. Morphological map

Our morphological map of western Tempe Terra is shown in Fig. 2. Type examples of unit morphologies are listed in Fig. 3, according to inferred stratigraphic order from youngest (Fig. 3A) to oldest (Fig. 3L). Cross sections with inferred stratigraphic relationships are shown in Fig. 4.

The *highland unit* (*Hld.*, Fig. 3L) is the stratigraphically oldest unit and forms a central massif. It is heavily fractured and extensional normal faulting has formed tectonic graben. The ~1000–3200 m elevation massif is largely overlain by surficial deposits (Fig. 4), including the *apron unit* (*Apr.*, Fig. 3C) and the *mantling unit* (*Mtl.*, Fig. 3B). The *apron unit* deposits occur on the massif's slopes and have convex topographic profiles (Fig. 4), a lobe-shaped planform appearance, and a meter-scale surface texture that is smooth, pitted, or ridged (Fig. 3C). Texturally similar deposits infill large impact craters (>3 km diameter). The *mantling unit* infills and smooths topographic lows of the massif and has a pitted surface texture (Fig. 3B).

Two flow units lie along the southeastern margin of the massif (the *upper flow unit, UFl.*, Fig. 3E; the *lower flow unit, LFl.*, Fig. 3F). The flows seem to have originated in the east of the study area based on their planform appearance, before pooling against the massif and diverging (shown by northeastward and southwestward pointing lobate margins; Fig. 2). The *upper flow unit* has a smooth surface texture and is near planar (mean elevation of 396 m with a standard deviation of 40 m). However, the flow has ~30 m high margins (Fig. 4A), and ~100 m wide fractures near its margins and around surface depressions interpreted as manifestations of topography (e.g., impact craters) underlying the unit (Fig. 5A and B). The *lower flow unit* is exposed along the margin of the *upper flow unit* and appears to underlie it (Figs. 4 and 5C). Notably, a ~200 m high scarp (Fig. 5A) and a possible mass-wasting feature comprising nested curvilinear blocks (Figs. 3F and 5A) appear to have back-wasted into the *lower flow unit*. At the base of the scarp, the *smooth unit* (*Smt.*, Fig. 3G) is exposed, which has an overall monotonous appearance with a faint etched/fractured texture.

Along the contact of the massif and flows, where the apron unit descends the massif, the *mound unit* (*Mnd.*, Fig. 3D) occurs. The unit consists of mounds with fractures along their crests (Fig. 5D) and irregular circular depressions with raised rims (Fig. 5E). The mounds are elongated, oriented roughly radially from the valley head, and the sinuous ridges appear to emerge from the mounds (Figs. 2 and 5A).

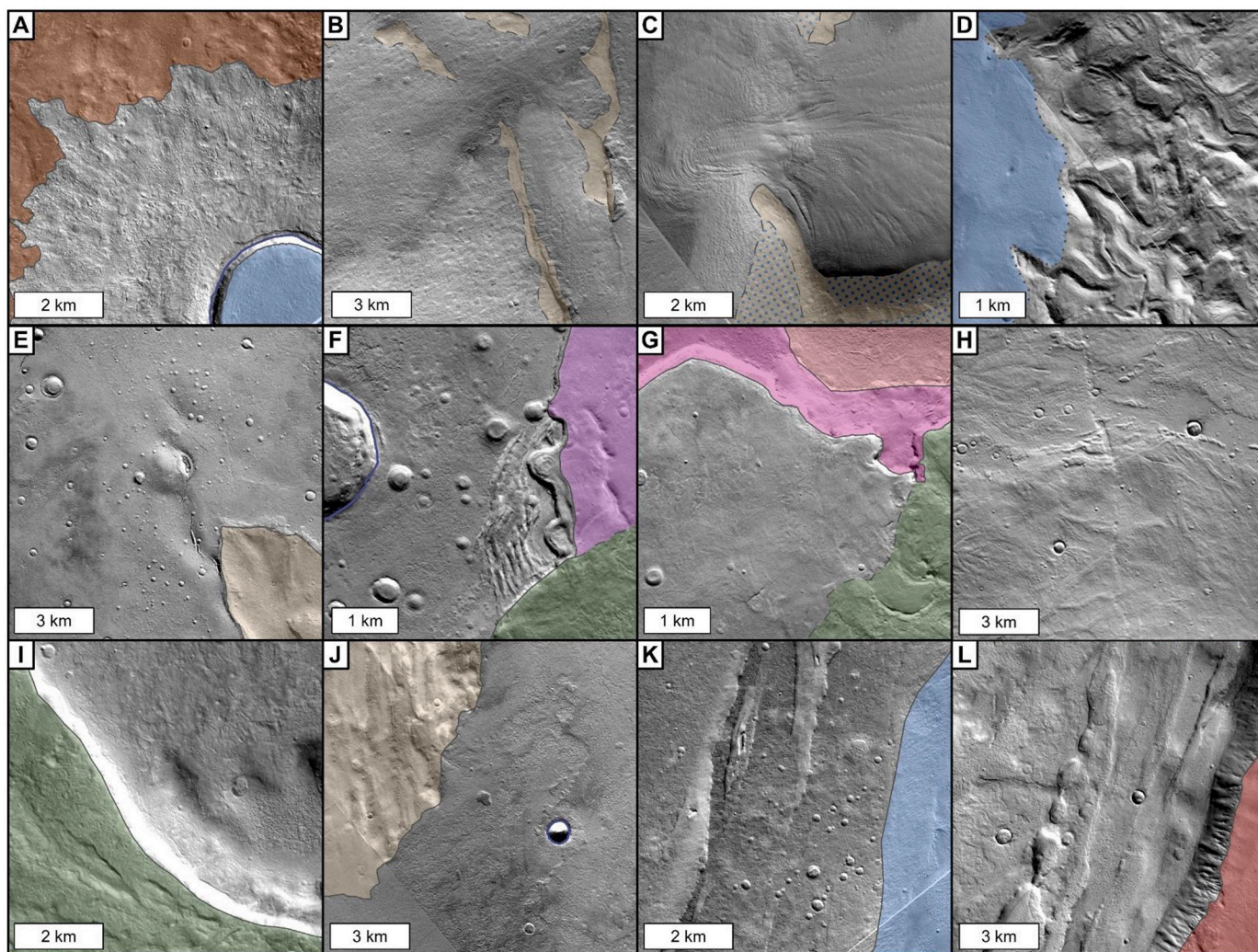East of the flow units lies the *ridged unit* (*Rgd.*, Fig. 3H), which forms a

Fig. 3. Geomorphic map units in west Tempe Terra. CTX images of the type locations of the geomorphic units from Fig. 2, with the subject unit left uncolored and surrounding units colored. Data types and product IDs are listed in Supplementary Materials 1. (A) Impact unit, *Imp.* (B) Mantling unit, *Mtl.* (C) Apron unit, *Apr.* (D) Mound unit, *Mnd.* (E) Upper Flow unit, *UFl.* (F) Lower Flow unit, *LFl.* (G) Smooth unit, *Smt.* (H) Ridged unit, *Rgd.* (I) Mesa unit, *Msa.* (J) Rift Fill unit, *RFl.* (K) Plains unit, *Pln.* (L) Highland unit, *Hld.*
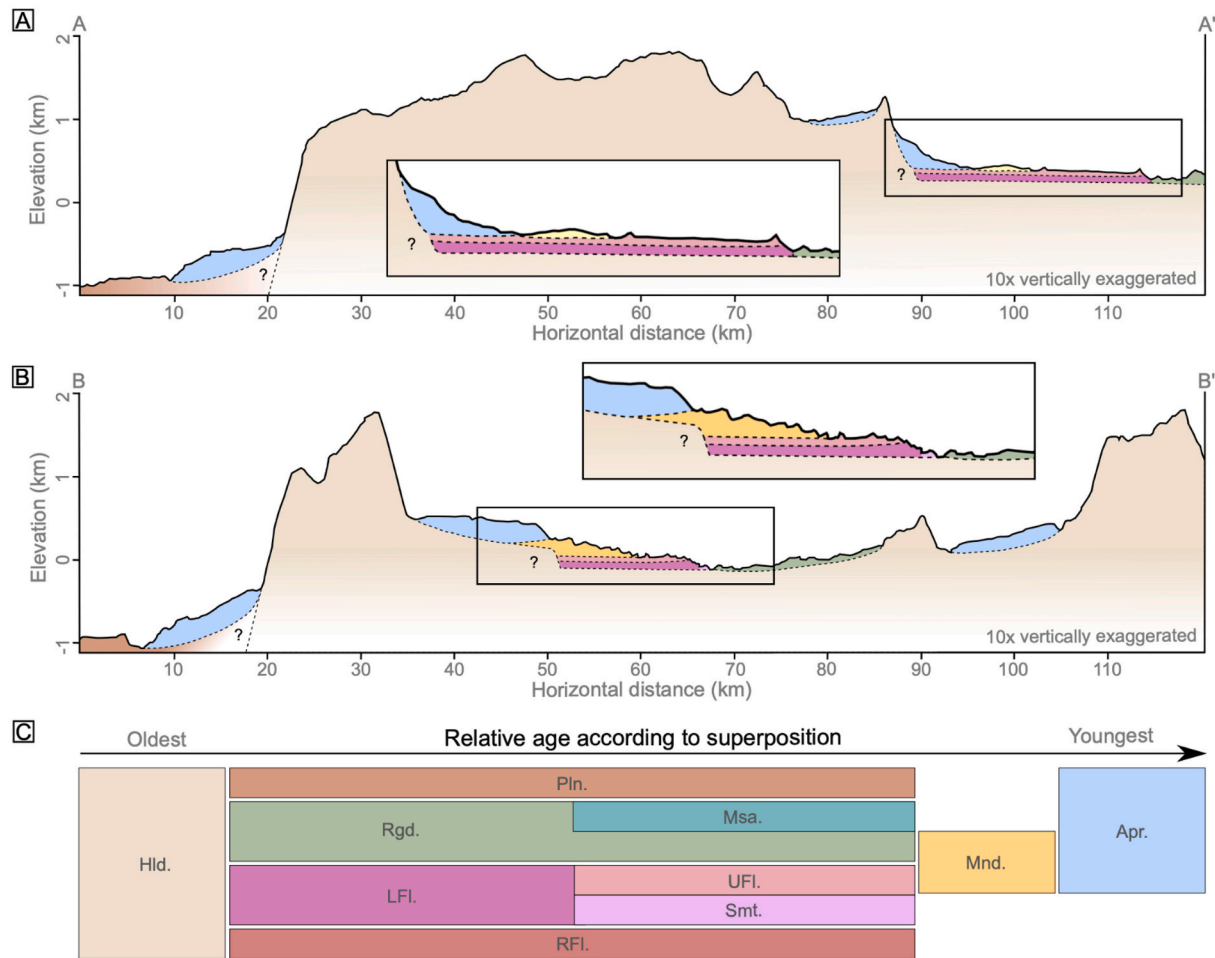
Fig. 4. Schematic cross section A-A' and B-B' and stratigraphic relationships of units. Cross section A-A' (A) and B-B' (B) shown on the geomorphic map in Fig. 2. The surface topography is extracted from an HRSC DEM, but subsurface contacts and unit thickness are inferred from the topography and observed stratigraphic relationships. (C) Stratigraphic relationships of the geomorphic map units. The columns represent relative unit ages according to superposition, but the relative ages between rows could not be determined. The size of boxes is schematic and not representative of length of time.

gently northwest-dipping plain. The unit has an etched appearance and shows evidence of topographic inversion including sinuous ridges (Fig. 5C) that are stratigraphically separated from Systems I and II by both the lower and upper flow units (i.e., older and genetically unrelated; Fig. 4). Enclosed within the *ridged unit* lie two prominent ~200 m-high mesas (the *mesa unit, Msa.*, Fig. 3I). The mesas are aligned along a depressed central 'spine' and the larger of the two is surrounded by a ~20 m-deep and ~0.5 km-wide moat (Fig. 5A and F).

4.2. Sinuous ridge age estimation

In the homogenous 1650 km^2 count area in the *upper flow unit* (Fig. 6A), we digitized 496 impact craters with diameters >120 m. Topographic depressions, interpreted as impact craters predating the flow, were excluded from the count. We found a best-fit isochron of 1.0 ± 0.1 Ga for 49 craters with diameters between 300 and 900 m (Fig. 6B). In the 453 km^2 count area in the *apron unit* (Fig. 6A), we digitized 311 impact craters with diameters >50 m. We found three best-fit isochrones (Fig. 6C) of 30 ± 2 Ma (160 craters), 220 ± 40 Ma (18 craters), and 3.0 ± 1 Ga (5 craters). All but one of the five craters fitted to the 3 Ga isochron appear to pre-date the surface of the apron unit so we exclude this isochron from further analyses.

4.3. Sinuous ridge 2D morphometry

Sinuous ridge System I overlies the *upper flow unit* and originates in the *mound unit* (Fig. 7A and B). System I has an interpolated length of 3.9 km with a sinuosity of 1.10. It comprises three segments (Fig. 7B): segment 1 (843 m long, sinuosity of 1.09) runs along and across a mound of the *mound unit*; segment 2 (2408 m long, sinuosity of 1.10) is narrow at the start and end but grows broader in the middle and has a small branch that bypasses the main ridge; and segment 3 (518 m long, sinuosity of 1.08) is a narrower ridge that gradually narrows and lowers, before tapering out.

Sinuous ridge System II lies in a ~3 km broad low-relief valley within the *lower flow unit* (Fig. 7C and D). System II has an interpolated length of 4.8 km with a sinuosity of 1.17. It consists of two segments (Fig. 7D); segment 1 (1396 m long, sinuosity of 1.28) forms a narrow ridge, segment 2 (2988 m long, sinuosity of 1.10) starts narrow and transitions into a wider, multi-crested ridge with a lateral fan, and terminates in a fan-shaped deposit comprising multiple narrow, divergent ridges.

4.4. Sinuous ridge morphology & 3D morphometry

We subdivided System II into four morphological zones (Fig. 8). These morphological zones are independent of segments and are based on visual planform appearance and crest topography. Zone I is a narrow, symmetric, and sharp-crested ridge with a pitted appearance of the crest
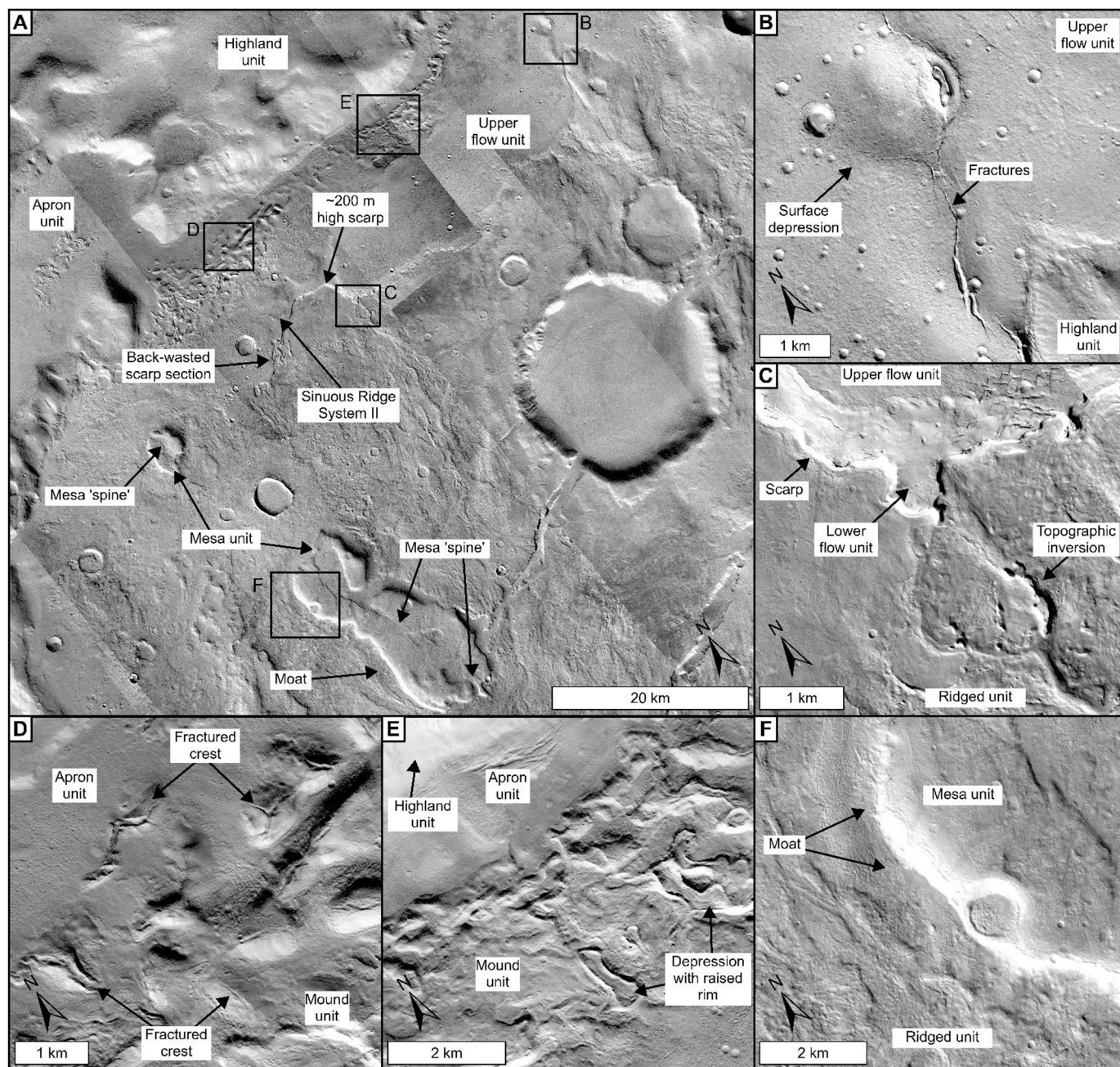
Fig. 5. Features and landforms in west Tempe Terra. CTX images with key features labelled. Data types and product IDs are listed in Supplementary Materials 1. (A) The landscape surrounding Sinuous Ridge System II, with boxes showing the location and extent of panels B to F. (B) Surface depressions and fractures in the upper flow unit due to structures underlying the flow. (C) Topographic inversion of the ridged unit. (D) Fractured crests of mounds in the mound unit, draped by the apron unit. (E) More complex mounds and structures forming the mound unit, including depressions with raised rims. (F) The contact between the ridged unit and the mesa unit, showing a moat surrounding the mesa.

and surrounding material (Fig. 8C). Zone II is similarly narrow, symmetric, and sharp-crested, but with an ambiguous, low-relief ridge at the north-eastern side of the central crest (Figs. 7D and 8D). Zone III has a lateral fan of approximately 0.3 km^2 on the south-western side of the ridge. Transects (Fig. 8E) show a multi-crested ridge, a convex lateral bulge, and the ambiguous ridge (starting in Zone II; Fig. 7D). Polygonal fracturing, 20–40 m wide, is seen on the surface of the lateral fan and crosscuts the ridge crest (Fig. 8A). A sudden drop in elevation at the end of Zone III commences Zone IV. Zone IV forms a terminal fan and the central crest becomes indistinguishable as it diverges into numerous minor ridges (Fig. 8F). The ridge crest elevation profile (Fig. 8B) reveals a noticeable trend of increasing height over Zone II and III and a sudden

height drop of 7.8 m at the transition of Zone III to IV.

System II has a width range of 46–687 m, with a median width of 107 m. The height, width, and width-height ratio for each morphological zone is shown in Fig. 9. The widths of Zones III (including lateral fan) and IV (including terminal fan) are larger than those of Zones I and II by a factor of approximately five. The greatest widths occur in Zone III (median width of 501 m) and visual inspection of the Zone III central multi-crested ridge (i.e., excluding the lateral fan) suggests that this portion of the central ridge is the widest of any section of System II. Heights are not as variable as widths; System II has a height range of 2–21 m and a median height of 8 m. Zone I has the smallest mean height of 5 m, compared to Zone II (12 m), Zone III (16 m), and Zone IV (10 m).
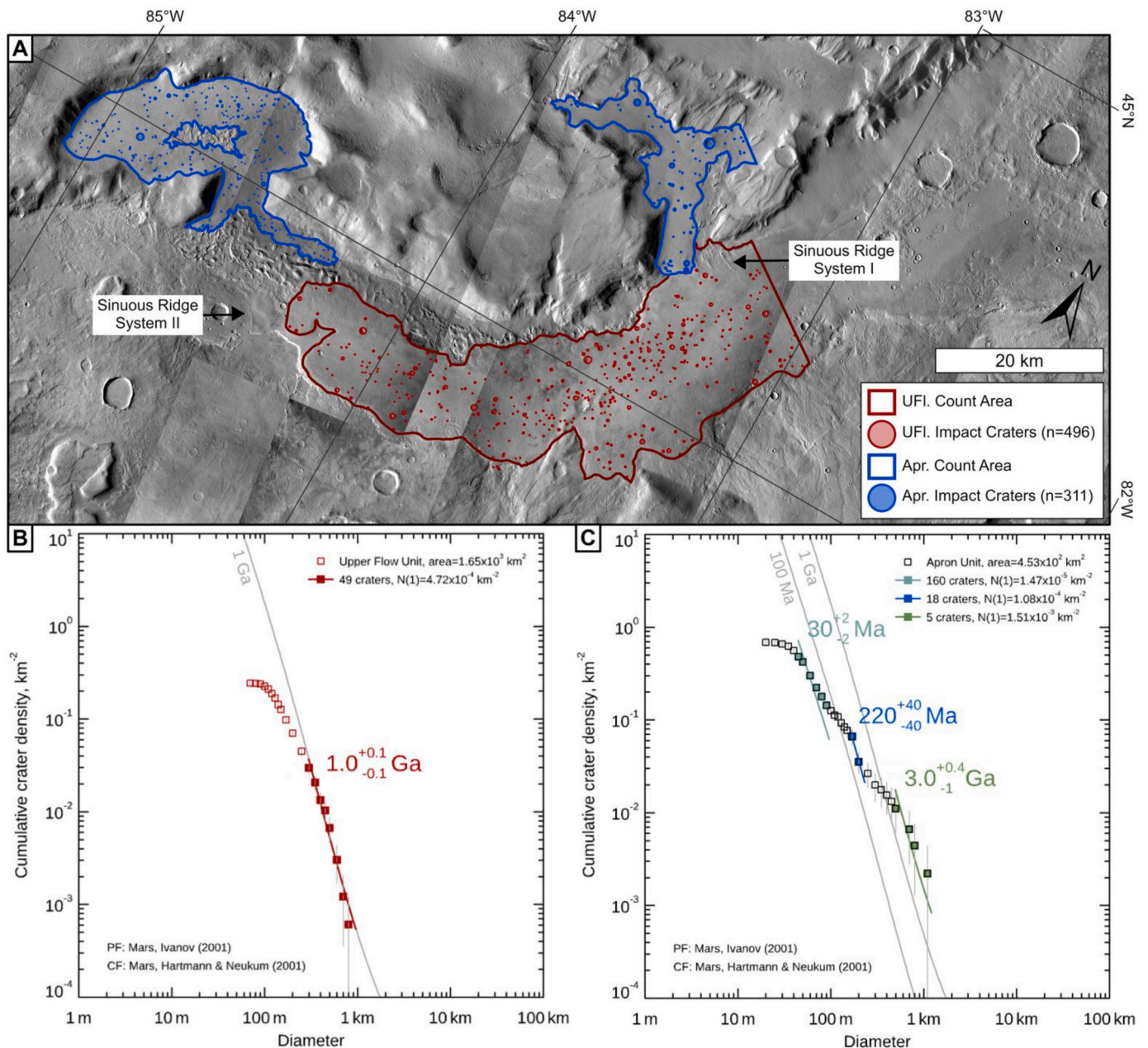
Fig. 6. Impact crater size-frequency distribution for areas of the Upper Flow unit and the Apron unit. (A) CTX map of the count areas used to derive the crater size-frequency statistics. Data types and product IDs are listed in Supplementary Materials 1. (B) The Upper Flow unit follows an age isochron of 1.0 ± 0.1 Ga, based on the best fit for 49 craters with diameters between 300 and 900 m. The x-axis is log incremental (Hartmann, 2005) and modelled ages are based on the Ivanov (2001) production function and the Hartmann and Neukum (2001) chronology function. (C) The Apron unit follows three age isochrons, a 30 ± 2 Ma isochron based on the 160 craters with diameters between 45 and 95 m, a 220 ± 40 Ma isochron based on 18 craters with diameters between 160 and 230 m, and a 3.0 ± 1 Ga isochron based on 5 craters with diameters between 500 and 1200 m.

Width-height ratios of System II range between 7 and 51. Zone II has the lowest median width-height ratio of 9. This is in stark contrast to Zone IV, which has a mean width-height ratio (42) that is more than four times higher. Heights and widths are positively correlated and, within each zone, are best described by linear fits (Fig. 9D).

5. Interpretations

5.1. Map unit interpretations

We interpret the *highland unit*, which forms the ancient and heavily deformed massif, as bedrock. It broadly corresponds to the globally mapped *Middle Noachian Highland Unit* (sedimentary and volcanic materials; 3.84–3.94 Ga; Tanaka et al., 2014a, 2014b), and is dissected by large Noachian tectonic graben (Hauber et al., 2010).

The massif is almost entirely overlain by the *apron unit* and *mantling unit* (Fig. 2), which we interpret as ice-containing Amazonian deposits. The *apron unit* consists of Viscous Flow Features (VFFs; Milliken et al., 2003; Squyres, 1979) that are widely interpreted as debris-covered glaciers (Head et al., 2010; Holt et al., 2008; Levy et al., 2010b; Petersen et al., 2018). This is supported by close morphological similarities to VFFs across Mars' mid latitudes, including convex-upwards topographic profiles (Fig. 4) suggestive of internal deformation, pitted textures suggestive of sublimation, and surface texture of ridges and
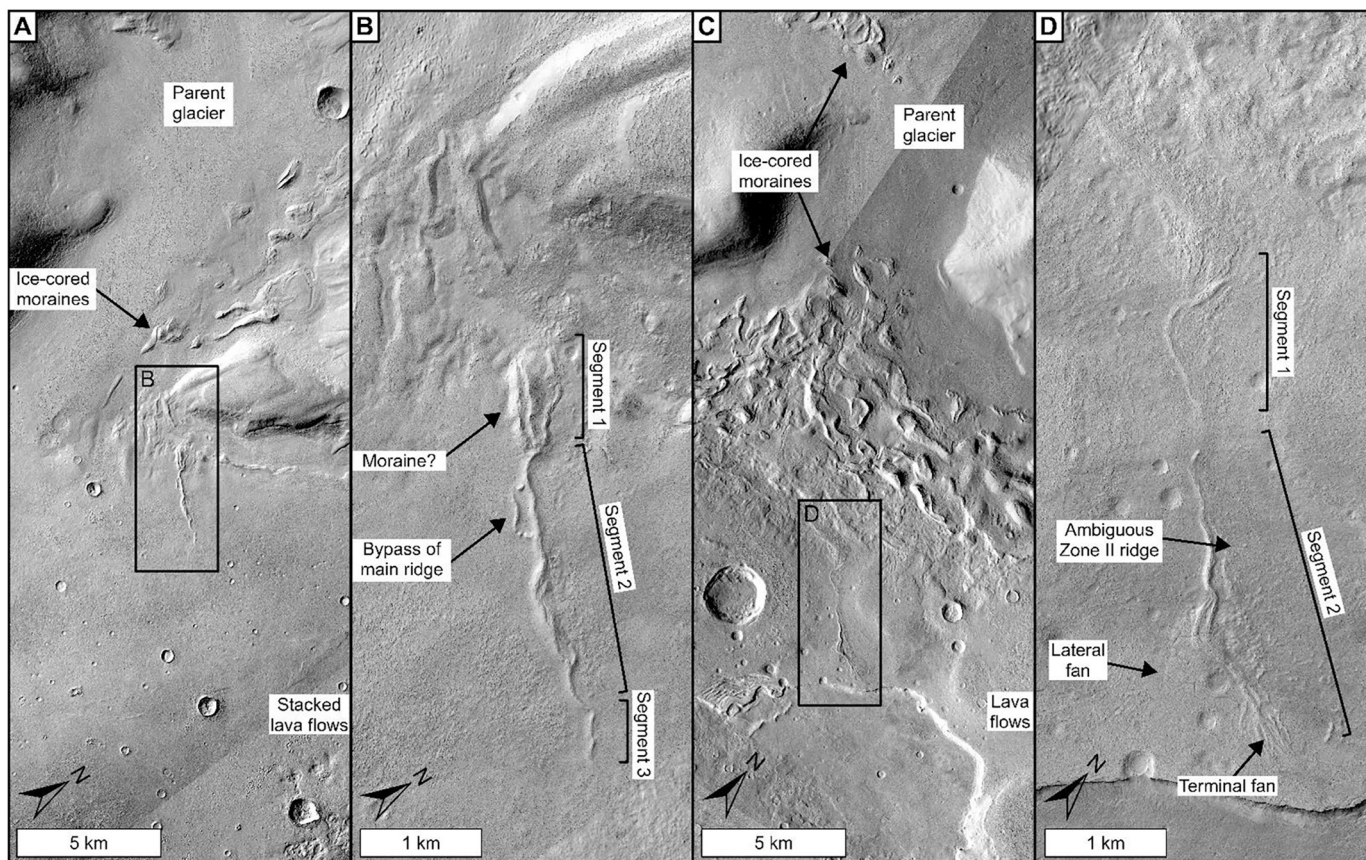
Fig. 7. Sinuous ridge Systems I and II. Key features are labelled, based on interpretations stated in Section 5.1. Data types and product IDs are listed in Supplementary Materials 1. (A) CTX mosaic of System I. (B) HiRISE image of System I. (C) CTX mosaic of System II. (D) HiRISE image of System II.

furrows (Fig. 3C) suggestive of flow (Head et al., 2010; Squyres, 1979). Our interpretation is also supported by morphological comparison to VFFs that have been confirmed to have high subsurface ice purity based on SHARAD observations (Holt et al., 2008; Petersen et al., 2018).

The *mantling unit* is the stratigraphically youngest unit, which we suggest may be a layered air-fall deposit with possible ice content, such as Latitude-Dependent Mantle (LDM; Head et al., 2003). This interpretation is based on topographic smoothing (Fig. 3B) which is suggestive of recent airfall layer(s) draped on older pre-existing topography (Mustard et al., 2001). If the deposit is analogous to the LDM, it likely formed in recent ice ages (0.4–2.1 Myr; Head et al., 2003) during periods of higher orbital obliquity when obliquity-driven insolation changes redistributed water-ice to the mid-latitudes (Schon et al., 2009).

The *upper flow* and *lower flow* units lie along the eastern and southeastern margin of the massif. The most likely interpretation is that these units are stacked lava flows, with the *lower flow unit* being an old lava flow which is overlain by the younger *upper flow unit* (Figs. 4 and 5C). A lava origin is supported by the lobe-shaped planform appearance and surface morphology of the flows (Fig. 5B). The contact between the *upper flow unit* and the *smooth unit* is a scarp (Figs. 2 and 5A), which we interpret as an erosive feature that has undergone some degree of induration and back-wasting. The flows could alternatively be mud flows as these could produce similar morphologies to lava under Martian surface conditions, according to laboratory experiments (Brož et al., 2020a, 2020b). For example, the observed raised outer margin of the *upper flow unit* (Fig. 4A) can form by inflation and subsequent deflation of mud or lava flows (e.g., Wilson and Mouginis-Mark, 2014). We consider a lava flow origin for the *upper* and *lower flow units* to be more probable considering the location of the site within a province containing widespread evidence for volcanism.

The *mound unit* forms the contact between the VFFs and the lava flows (Figs. 2 and 4B). We propose two possible formation hypotheses for the mounds: (1) the mounds are VFF-related and are stagnant ice features, or (2) the mounds are lava flow related deformation features. We favor the first hypothesis and suggest that the elongated mounds are ice-cored moraines mantled by supraglacial material, which formed during deglaciation. Under this interpretation, the cracked crests of the mounds (Fig. 5D) are interpreted to be collapse features arising from internal mass loss of ice cores. Morphologically similar features elsewhere on Mars have been attributed to ice loss (e.g., Baker and Head, 2015; Pierce and Crown, 2003), strengthening our interpretation. The second hypothesis, is that surface folding and buckling of the lava flows due to flow-parallel compression resulted in regularly-spaced folds with a corrugated surface appearance (Deardorff et al., 2019; Gregg et al., 1998). We discount this second hypothesis as some mounds occur ~250 m up-valley (Fig. 2) which is too far up-slope for the lava flows to have reached (Fig. 7A and C), and are closely spatially associated with the VFFs.

The *ridged unit* is complex and its emplacement and modification is likely influenced by multiple processes. The irregular terrain in the southeast of the study area, surrounding a ~20 km diameter impact crater, is likely remnants of highly eroded impact ejecta. Inverted channels, which could be volcanic or fluvial in origin, are eroding out of an overlying layer. This topographic inversion (Fig. 5C) suggests that extensive landscape erosion occurred during the region's history. However, the clear stratigraphic separation of the *ridged unit* from the younger sinuous ridge Systems I and II, and a lack of evidence for topographic inversion postdating the upper and lower flow units (which overlie the ridged unit and underlie sinuous ridge Systems I and II) means that regional topographic inversion pre-dates the formation of the VFF-linked sinuous ridges. Enclosed within the *ridged unit*, lie two mesas which form the *mesa unit*. The simplest interpretation of these
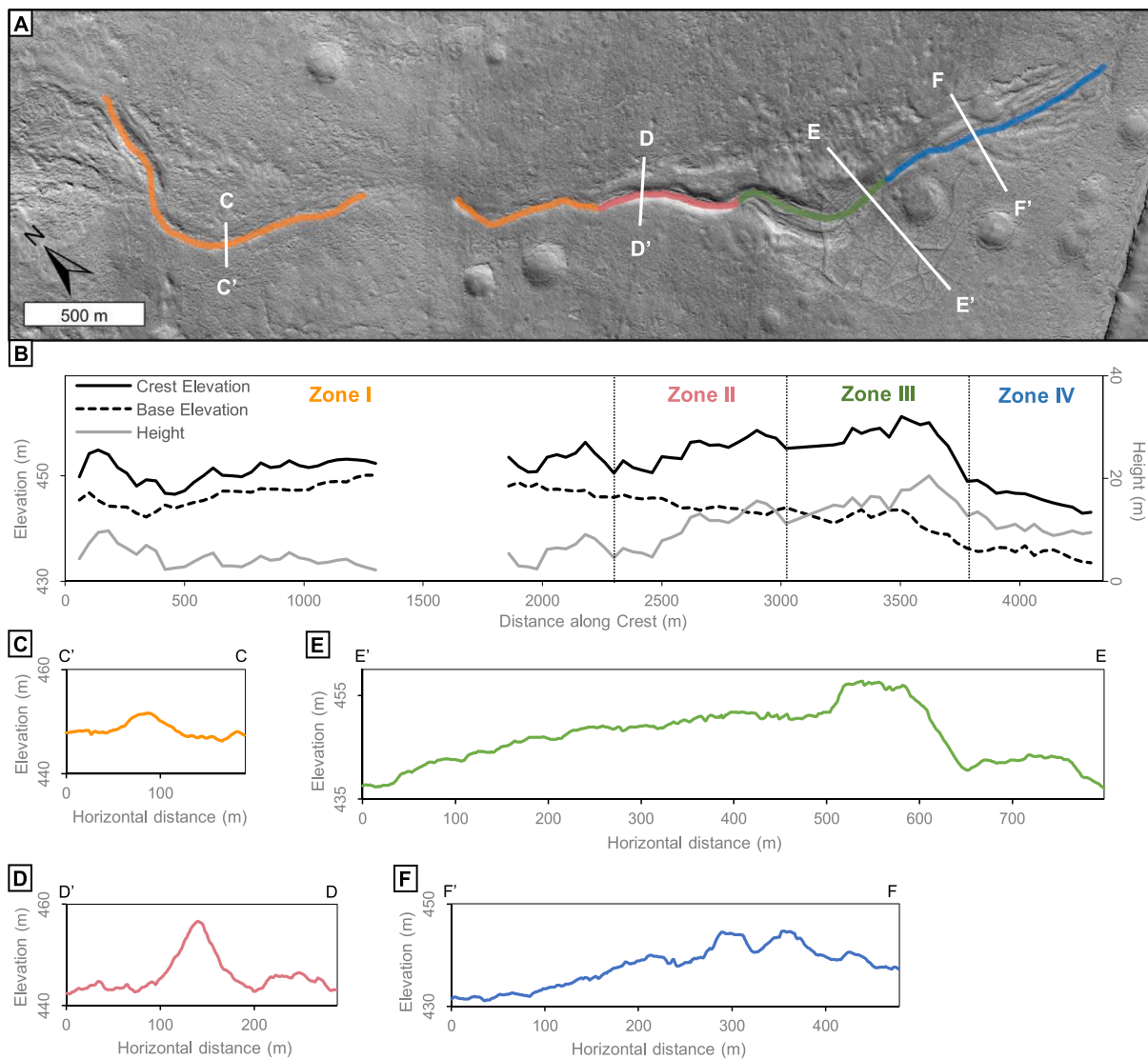
Fig. 8. 3D Ridge Morphometry of System II in west Tempe Terra. (A) HiRISE image of the ridge crest line of System II, subdivided into four morphological zones. Data types and product IDs are listed in Supplementary Materials 1. (B) Crest elevation, base elevation, and ridge height from HiRISE DEM. Data points are taken every ~40 m along ridge crest. Data 'gap' represents the distance between Segment I and II. Ridge height is calculated as the difference between crest and base elevation. (C–F) Representative topographic profiles from HiRISE DEM for morphological Zone I (C′-C), Zone II (D′-D), Zone III (E′-E), and Zone IV (Zone F′-F).

mounds is that they are lava mesas with a central spine due to the igneous intrusion or faulting. A less likely hypothesis, but one which better represents the mounds' surrounding moat and central spine (Fig. 5A and F), is that the mounds formed by volcano-ice interaction. Volcanic intrusion below a paleo ice sheet or frozen lahar can form flat topped mounds, called möberg ridges, aligned along a central fissure (e. g., Galaxias Mons; Allen, 1979; Pedersen, 2013).

5.2. Sinuous ridge age constraints

The 220 ± 40 Ma crater retention isochron of the *apron unit* (Fig. 6C) is broadly in line with age estimates of VFFs in Tempe Terra (~110–200 Ma; Butcher et al., 2017; Van Gasselt et al., 2011). Similarly, the 30 ± 2 Ma isochron (Fig. 6C) matches that proposed to reflect an ice-rich mantling deposit superposing the VFFs in the region (Butcher et al., 2017; Van Gasselt et al., 2011), and thus may represent a minor resurfacing event.

The crater retention age of 1.0 ± 0.1 Ga for the *upper flow unit* (Fig. 6B) seems reasonable considering similarly young Amazonian lava flows have been identified 1000 km to the SE in Kasei Valles (~1.3 Ga;

Hepburn et al., 2020). However, we note that this crater retention age could be an underestimation caused by erosion of impact craters or the flow surface being shielded from impacts by the VFFs during more extensive glaciation.

We constrain the formation ages of System I to between 220 Ma and 1 Ga, and suggest that this age constraint is also applicable to System II. Although System II overlies the *lower* instead of the *upper flow unit*, both systems have similar relationships to VFFs and appear equally preserved. The limited spatial extent of the *upper flow unit* – which does not reach as far south as System II – means that both ridges may postdate it (Fig. 6A). Thus, we suggest that Systems I and II are Amazonian in age, and formed at broadly similar times between 220 Ma and 1 Ga – possibly even simultaneously.

5.3. Sinuous ridge formation hypotheses

Although it is conceivable that the two ridges have a different origin, their apparent morphological, morphometric, stratigraphic, and contextual similarities make this improbable. Numerous formation hypotheses for Martian sinuous ridges have been proposed, including
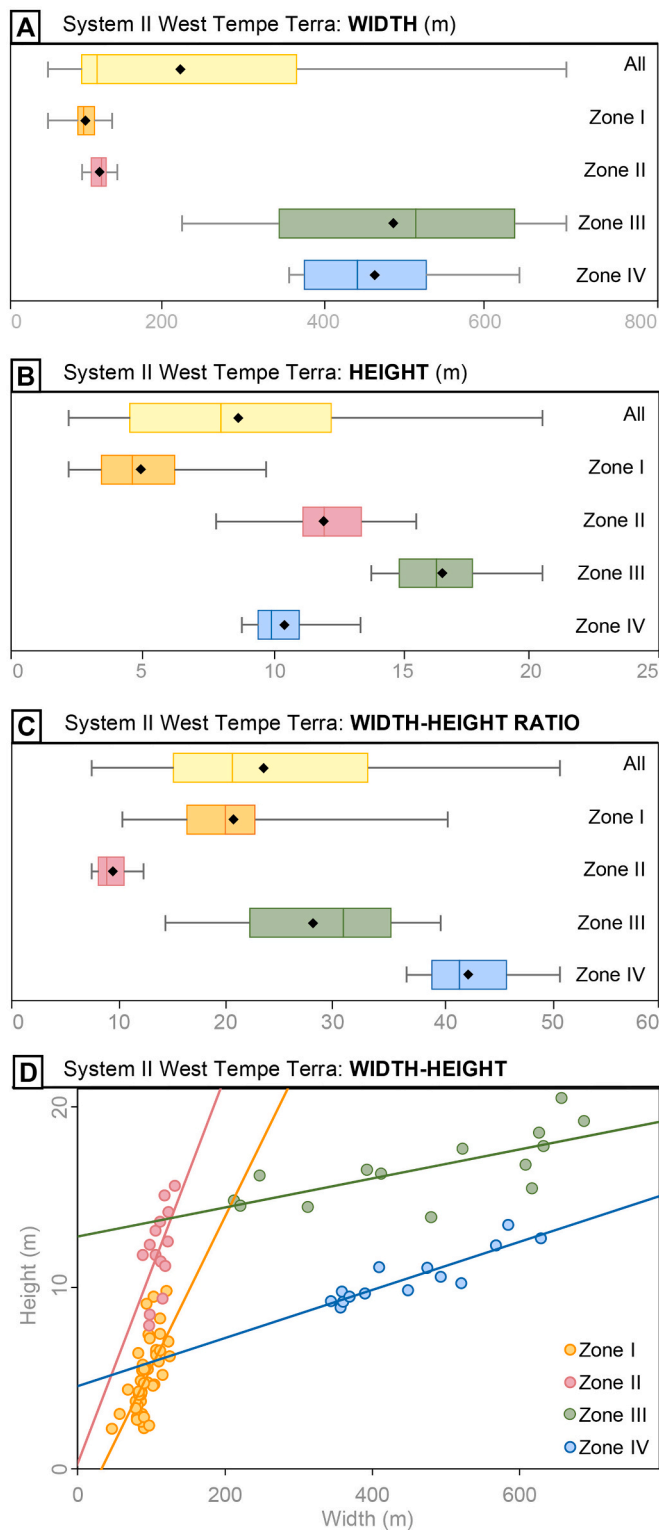
Fig. 9. 3D morphometries of System II in west Tempe Terra, subdivided by morphological zones. (A-C) Boxplots of 3D measurements of All Zones ($n = 90$), Zone I ($n = 48$), Zone II ($n = 14$), Zone III (n = 14), and Zone IV (n = 14). The boxes are the interquartile range with a separation line representing the median, whiskers represent minimum and maximum values, and diamonds represent the mean values. (D) Scatterplot of heights and widths of sinuous ridge System II. Solid lines are linear fits for each zone. Height and width measurement uncertainty whiskers are too small to display, but their extent falls within the point symbols.

eskers, moraines, inverted fluvial paleochannels, and igneous features (e.g. Banks et al., 2009; Bernhardt et al., 2013; Burr et al., 2009; Butcher et al., 2017, 2020). In this section, we discuss which formation hypothesis is supported by our observations of the morphology, stratigraphy, and consilience with the contextual landscape.

5.3.1. Subglacial origin

Eskers are formed by glaciers and are sedimentary ridges that are deposited by meltwater in subglacial conduits (e.g., Shreve, 1985). In terrestrial glacial landscapes, eskers have highly variable morphologies (Storrar et al., 2015) and can be associated with other glacial landforms such as moraines and kames (e.g., Benn and Evans, 2010; Ingólfsson et al., 2016). The association of the two sinuous ridges with glacial landforms (putative debris-covered glaciers and possible ice-cored moraines; Fig. 7) is consistent with an esker hypothesis. The System II lateral fan (Figs. 7D and 8E) could be evidence of a rapid, high flow-power event (e.g., a glacial outburst flood) where the conduit cannot accommodate discharge by wall melting (Gorrell and Shaw, 1991; Bernhardt et al., 2013), causing incursion of meltwater under the ice and into lateral cavities. The following observed characteristics of the ridges further support an esker origin; (1) System II has reaches which ascend topography (Fig. 8B), a common characteristic of eskers formed in pressurized subglacial conduits (Shreve, 1985); (2) the 'bypass' in System I (Fig. 7B) is similar to an esker bypass, which form by increasing hydraulic pressure causing meltwater and sediment to debouch from the main conduit and form lateral fans or minor tunnels (Burke et al., 2012; Gorrell and Shaw, 1991); and (3) the terminal fan of System II (Fig. 7D), which is similar to subaerial terminal fans that form on terrestrial eskers (Brennand, 2000). Furthermore, the only process that we find evidence of, after the emplacement of the flow unit ~1 Ga, is glaciation. Considering that two VFFs within this graben system have sinuous ridges emerging from them (or three, including northwest Tempe Terra; Butcher et al., 2017), we favor the glacial hypotheses. We find that our observations of the sinuous ridge morphology, stratigraphy, and consilience with the contextual landscape best support the esker hypothesis for both sinuous ridges.

We compare the system and segment morphometry of the sinuous ridges in western Tempe Terra, to eskers elsewhere on Mars and Earth (Figs. 10 and 11) to determine if the sinuous ridges are morphometrically similar. We compare the 2D morphometries of System I and II to eskers in Canada (Storrar et al., 2013, 2014), and candidate eskers on Mars in Phlegra Montes (Butcher, 2019; Gallagher and Balme, 2015) and northwest Tempe Terra (Butcher et al., 2017, 2020). The Canadian eskers formed during deglaciation of the Laurentide Ice Sheet during the early Holocene and comprise 7027 esker systems, or 20,712 segments (Storrar et al., 2014). The candidate esker complex in Phlegra Montes is interpreted to have formed ~150 Ma due to basal melting of a VFF (Gallagher and Balme, 2015) and comprises 22 esker systems and 38 segments (Butcher, 2019). The candidate esker in northwest Tempe Terra is interpreted to have formed ~110 Ma due to basal melting of a contemporary VFF (Butcher et al., 2017), possibly in multiple episodes (Butcher et al., 2020). The Martian esker comparison focuses on Amazonian-aged VFF-linked candidate eskers in Mars' mid-latitudes and thus excludes the early Hesperian-aged candidate eskers of the south circumpolar Dorsa Argentea Formation (e.g., Butcher et al., 2016) and Argyre Planitia (e.g., Banks et al., 2009).

The system lengths of the sinuous ridges in western Tempe Terra (4.8 km and 3.9 km) are slightly higher than those of Phlegra Montes (mean of 0.6 km), slightly lower than northwest Tempe Terra (17.1 km), and lie within the interquartile range of Canadian eskers (Fig. 10A). Segment lengths of the sinuous ridges in western Tempe Terra are also comparable to those observed on Mars and Earth (Fig. 10C). The ridge system sinuosities of western Tempe Terra (1.10 and 1.17) are very similar to that of northwest Tempe Terra (1.13) and lie between the median and maximum sinuosity values of Phlegra Montes and Canada (Fig. 10B). Overall, we find that the lengths and sinuosities of the
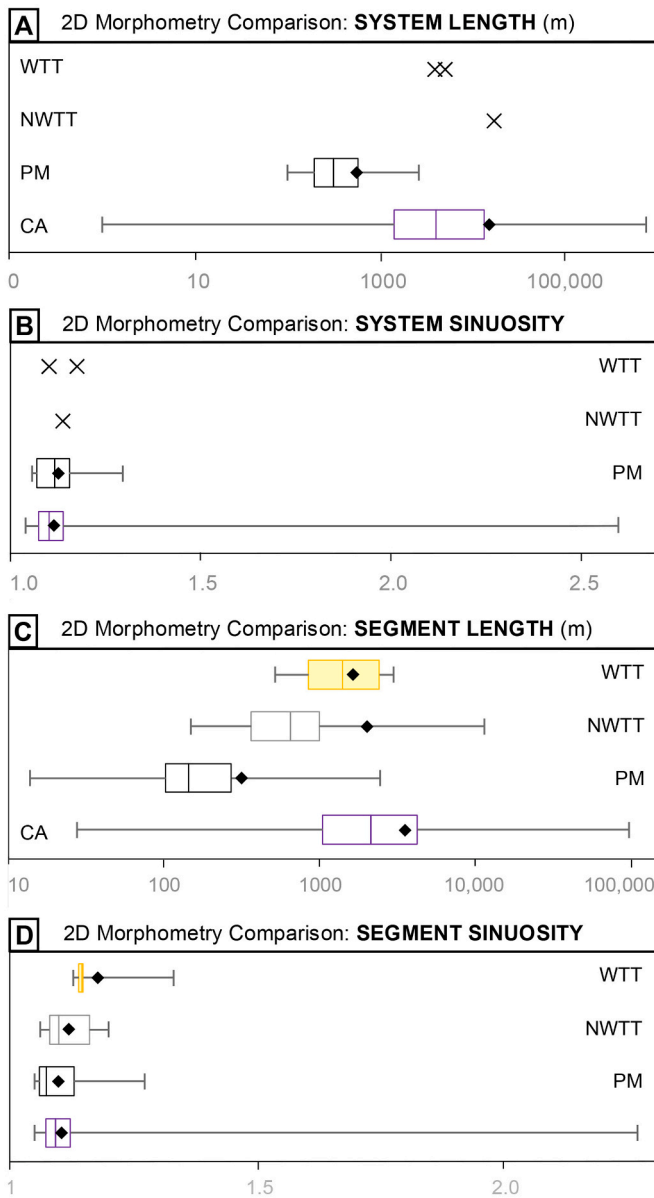
Fig. 10. **2D morphometries of eskers on Mars and Earth**. (A/B) The system lengths and sinuosities of western Tempe Terra (WTT, this study, $n = 2$), northwest Tempe Terra (NWTT, $n = 1$; Butcher et al., 2020), Phlegra Montes (PM, $n = 22$; Butcher, 2019), and Canada (CA; $n = 7027$; Storrar et al.,2014). (C/D) The segment lengths and sinuosities of WTT ($n = 5$), NWTT ($n = 8$), PM ($n = 38$), and CA ($n = 20,712$). The boxes are the interquartile range with a separation line representing the median, whiskers represent minimum and maximum values, and points represent the mean values. Note logarithmic axis of panels A and C.

sinuous ridges in western Tempe Terra are broadly similar to those of candidate eskers elsewhere in Mars's mid latitudes and on Earth (Fig. 10). As noted by Butcher (2019), the only values that show clear differences between the Martian and terrestrial eskers, are continuities; Martian esker systems have similar continuities between 0.91 and 0.96 while Canadian esker continuity values are considerably lower at 0.65 (Supplementary Materials 4). Erosion rates are significantly lower on Mars than on Earth (e.g., Carr and Head, 2010) and terrestrial factors, such as vegetation and water, enhance erosion. Thus, the difference in continuity might be attributable to varying post-depositional processes which cause esker fragmentation and lower continuities on Earth than on Mars (Butcher, 2019).
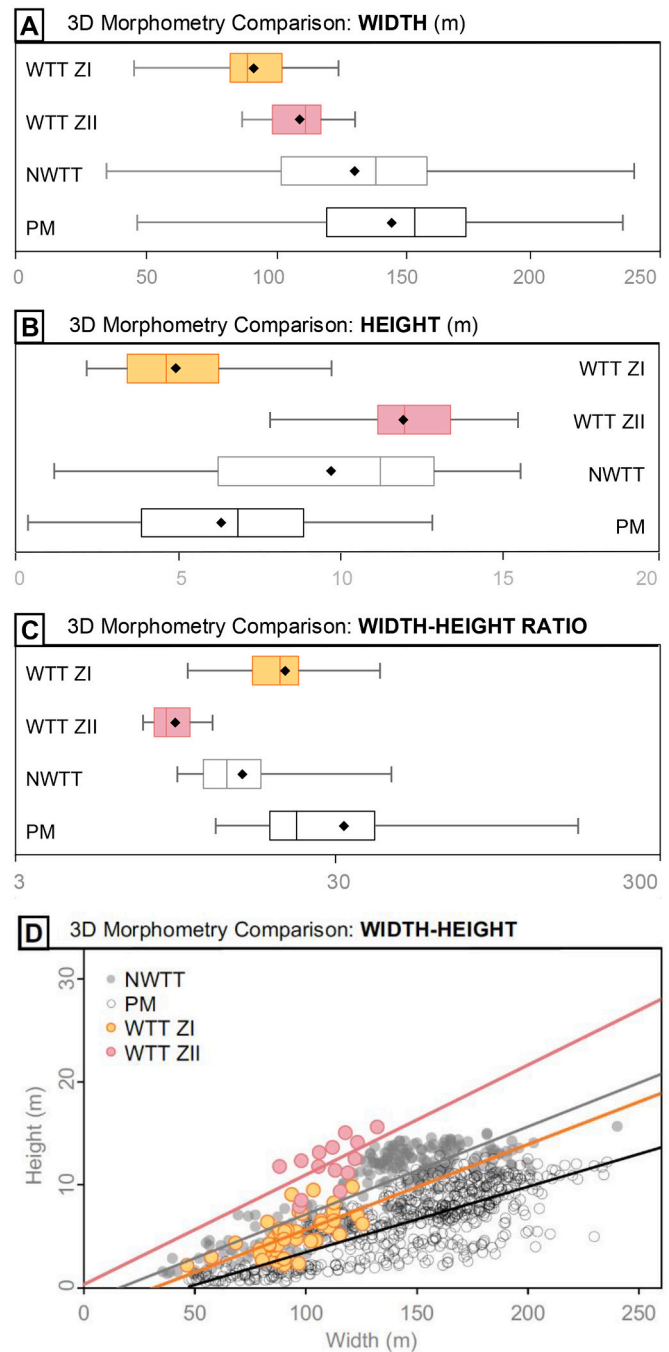

Fig. 11. **3D morphometries of other Martian eskers compared to System I in west Tempe Terra**. Shown are west Tempe Terra Zone I (WTT I, $n = 48$), west Tempe Terra Zone II (WTT II, $n = 14$), northwest Tempe Terra (NWTT, Subzone IV, $n = 237$; Butcher, 2019) and Phlegra Montes (PM, $n = 582$; Butcher, 2019). (A-C) Boxplots of height, width, and width-height ratio. Note logarithmic axis of panel C. The boxes are the interquartile range with a separation line representing the median, whiskers represent minimum and maximum values, and diamonds represent the mean values. (D) Scatterplot of heights and widths of eskers. Solid lines are linear fits for each zone, with line colors corresponding to point color in legend.

Due to limited existing 3D datasets of eskers on Earth, comparison of 3D morphometries is restricted to candidate eskers in Mars' mid latitudes (Fig. 11). The comparison of 3D morphometries of sinuous ridges in west Tempe Terra is limited to System II, Zones I and II, as there is no appropriate analog for the lateral and terminal fans of Zone III and VI (Fig. 8) in pre-existing datasets of Martian esker morphometries, making

these zones unfit for comparison. Zone II has an ambiguous ridge north of the central crest (Figs. 7D and 8D), which for the purpose of this study was not ascribed as part of the candidate-esker (the central crest was assumed to be a stand-alone crest). Interpretation of the nature of this ambiguous ridge is complicated by sediment overlying the ridge, but there are multiple possibilities for its origin. An incised 'moat' could have formed due to erosion, dividing a single ridge into the current two ridges. Alternatively, the ambiguous ridge could be a secondary crest and material is infilling the zone between the two crests. The ridge could also simply be a happenstance pre-existing feature in the landscape. The northwest Tempe Terra esker has been interpreted as a composite of two 'stacked' eskers formed by multi-stage flow (Butcher et al., 2020). Therefore, we only use Subzone IV (the sharp-crested, non-stacked section) of the northwest Tempe Terra esker for comparison. Overall, we find the 3D morphometries of the Martian candidate eskers to be similar to the sinuous ridges in western Tempe Terra (Fig. 11).

Western Tempe Terra System II Zone I has a slightly lower typical width and height (but still within range) compared to the other Martian candidate eskers (Fig. 11A and B). However, this difference is proportional and the width-height ratio shows the interquartile range of Zone I overlaps with that of northwest Tempe Terra and Phlegra Montes (Fig. 11C). Zone II is most comparable to the northwest Tempe Terra esker, with the width and height overlapping with the first and third quartile of northwest Tempe Terra respectively (Fig. 11A and B). For a given height, Phlegra Montes is the widest, followed by western Tempe Terra System II (Zone I) and northwest Tempe Terra (Fig. 11D). As suggested by Butcher (2019), this width difference between Martian eskers of similar height could be due to varying degrees of post-depositional erosion. The Phlegra Montes esker lies furthest from the terminus of its parent VFF, followed by west Tempe Terra, and lastly northwest Tempe Terra (which is still partially buried under its parent VFF). The distance from the VFF-terminus could reflect the duration over which post-depositional erosion has occurred, resulting in increased width-height ratios with increased distances from VFF-termini (Butcher, 2019). Alternatively, variations in width-height ratios could reflect differences in formation conditions.

The sinuous ridges in western Tempe Terra are morphometrically comparable to eskers identified elsewhere on Earth and Mars, further supporting our leading hypothesis that the sinuous ridges of Tempe Terra are eskers.

5.3.2. Alternative hypotheses for sinuous ridge formation

An alternative hypothesis considered is that the sinuous ridges are moraines. This is based on the association of the sinuous ridges with the *mound unit*, which we interpret as ice-cored moraines (Fig. 5D and E). However, the sinuous ridges have a distinct morphology that is dissimilar to the mounds, suggesting different processes or circumstances governed their formation. A lateral moraine origin is the leading alternative hypothesis for System I, based on the orientation of the sinuous ridges (parallel to palaeo ice-flow direction) and the lateral location of System I compared to the VFF (Fig. 7A). However, a moraine hypothesis does not adequately reflect the observed complexities of System II. The most straightforward scenario, which ascribes the same formation process to both sinuous ridges, is that they are eskers. However, we do not rule out the moraine hypothesis for System I. The difference in implication between the esker and moraine hypothesis is that moraines can form during cold-based glacial conditions without meltwater, while meltwater is required for esker to form.

Another alternative hypothesis is that the sinuous ridges' formation is related to the underlying unit interpreted as a lava flow. For example, distributary channels of lava flows can form flow-parallel sinuous ridge shaped plateaus with fan-shaped lobes (Crown and Ramsay, 2016), but this is not consistent with the flow-perpendicular orientation of the sinuous ridges. Alternatively, the ridges could be ice-confined subglacial lava flows, which form by subglacial igneous intrusion causing lava to exploit pre-existing meltwater tunnels (Hungerford et al., 2014).

Although this would explain an esker-like appearance, we observe no evidence of a point sources or volcanic edifices at the heads of either of the sinuous ridges. We also note that the subglacial lava flow hypothesis requires pre-existing meltwater conduits, such as those in which eskers are deposited. Thus, this hypothesis invokes an additional process of subglacial eruption which is unnecessary to explain the observations. We suggest both lava flow-related hypotheses are improbable due to the complexity of events required, and general lack of supporting observations.

The third alternative hypothesis is that the sinuous ridges are inverted fluvial paleochannels. Inverted channels are positive relief ridges that form due to preferential erosion of sediment surrounding a channel (e.g., Pain and Oilier, 1995). Some of the morphological features of the two sinuous ridges can be explained under the inverted channel hypothesis; fan complexes for example have been observed on terrestrial inverted channels (Burr et al., 2009; Doelling, 2002; Malin and Edgett, 2003). There is evidence of topographic inversion of the *ridged unit* (Fig. 5C) but not of the *flow units*. Stratigraphic relationships clearly separate the formation of the VFF-linked sinuous ridges and the inverted channels exposed in the *ridged unit*. The *upper flow unit* and *lower flow unit* stratigraphically overlie the *ridged unit*, and there is no evidence of topographic inversion and/or channel incision of these younger units. Furthermore, erosion rates required for extensive topographic inversion of the *ridged unit* mainly occurred in the Hesperian (Carr and Head, 2010) prior to the formation of the ~1 Gyr *upper flow unit*. Thus, we discount the inverted fluvial paleochannel hypothesis as the *upper flow unit* shows no evidence of topographic inversion and we find no evidence that fluvial activity occurred after the flow units were emplaced.

6. Proposed drivers for esker-forming meltwater

Our identification of two additional VFF-linked eskers in western Tempe Terra contributes to a growing body of evidence of wet-based glaciation in the mid-latitudes of Mars during the Amazonian period. This section considers the wider implications of these findings in the context of Mars' climatic and geological history.

We propose that the sinuous ridges in western Tempe Terra are eskers which formed in the following landscape evolution sequence: 1) the ~1 Gyr lava flow is emplaced; 2) a glacial phase commences and the highland massif is glaciated; 3) the cold-based parent-VFFs advance and minimally reach the distal ends of sinuous ridge Systems I and II; 4) meltwater is produced, at least transiently, at the beds of the parent-VFFs and the eskers are deposited in a warm-based or minimally polythermal regime; 5) the parent VFFs revert to a cold-based thermal regime; 6) during the last phase of VFF retreat, ice-cored moraines form; and 7) ice stagnation occurs ~220 Ma and the parent VFFs reach their current extent.

The timescale at which eskers form on Earth, and the duration of water production required for their formation, is still uncertain and likely varies between sites. By extension, the timescale of Martian esker formation remains highly uncertain. On Earth, there is evidence that some eskers were deposited within hours, for example under glacial outburst flood conditions (e.g., Burke et al., 2008). Other eskers may have required many years (perhaps decades to centuries) to form (e.g., Mäkinen, 2003; Livingstone et al., 2020). In western Tempe Terra, the high discharge environment required for esker formation might have occurred minimally over a matter of hours, but we cannot rule out esker formation via meltwater discharge over much longer timescales.

If the two sinuous ridges in western Tempe Terra are indeed eskers, then this indicates that wet-based glaciation occurred at multiple sites in Tempe Terra, at least transiently. These include three sites within a 150 km-wide area in west Tempe Terra (this study) and northwest Tempe Terra (Butcher et al., 2017; Butcher et al., 2020), and possibly a fourth, more distal site ~600 km away in Chukhung crater (Fig. 1B) in central Tempe Terra (Butcher et al., 2021). Substantial amounts of flowing

liquid water would be required to form eskers at these sites in the last 100s of Ma, during a period in which liquid water on Mars was scarce. This makes Tempe Terra an interesting area for further studies of Mars' recent paleo-environment, as VFF melting must have been caused by a surface and/or a subsurface Amazonian heat source that is not yet fully understood.

Discoveries of candidate eskers bring with them an implication that our understanding of Martian climate and glaciology is incomplete and not yet fully captured by current modelling. We need to understand better both the abundance and stability of surface water over the past 100s of Ma on Mars, particularly in the context of low atmospheric pressure and temperature, and given the impacts of variable obliquity on insolation and climate. We note, however, that even if atmospheric pressures during esker formation were similar to today, the pressure exerted on VFF beds by meters-to-hundreds of meters of overlying ice should have permitted liquid water stability in the subglacial environment if the requisite thermal conditions were attained. What remains unknown is whether basal meltwater was the sole contributor of meltwater to esker formation, or whether surface meltwater inputs were also required.

The age estimates for the candidate eskers in Tempe Terra are based on the crater-retention ages of their parent VFFs and are 110 Ma for northwest Tempe Terra (Butcher et al., 2017), 220 Ma for western Tempe Terra (two VFFs, this study) and 330 Ma for Chukhung crater (Butcher et al., 2021). These age estimates will differ from the true esker formation ages by the time taken for the parent VFFs to retreat to their present extents, and the duration of any subsequent reworking of VFF surfaces (e.g. downwasting by sublimation). The spatial proximity of the three candidate eskers in northwest Tempe Terra and western Tempe Terra leads us to consider the possibility that they formed at similar times, and perhaps simultaneously. The uncertainties in impact crater retention age modelling, and the fact that parent-VFF crater-retention age is used as approximation of esker age, means that the 110 Ma difference in age estimates between the sites does not necessarily rule out simultaneous esker formation. However, current techniques would not allow us to resolve such close temporal relationships between features. Given the greater distance between Chukhung crater and the northwest and western Tempe Terra sites (600 km), it seems less likely that candidate eskers in Chukhung crater formed simultaneously with those further west.

Locally elevated geothermal heating is one of the previously proposed heat sources for past basal melting, as the eskers in Phlegra Montes and northwest Tempe Terra both lie in grabens near large volcano-tectonic provinces (Butcher et al., 2017; Gallagher and Balme, 2015). Modelling of the temperature at the base of VFFs by Butcher et al. (2017) found that under optimal conditions (surface temperature >215 K and ice thickness >1100 m), basal temperatures of 273 K can be produced if the geothermal heat flux is high (>0.08 Wm^{-2}) as can be the case in the vicinity of near-surface magmatic activity. The two newly-identified candidate eskers in west Tempe Terra lie in grabens, which is consistent with a geothermal heating hypothesis. However, these identifications also complicate the local geothermal heating hypothesis, as multiple, spatially distributed geothermal events would be required within the Tempe Terra region. Multiple, temporally separate drainage events might have contributed to the morphological complexity of the northwest Tempe Terra esker, but changing drainage dynamics within a single event was deemed a simpler explanation (Butcher et al., 2020). Alternatively, if esker formation was simultaneous across the northwest and western Tempe Terra sites (covering a region ~150 km wide), a more widespread regional geothermal heating event could be required. In the absence of additional evidence for such widespread regional geothermal activity as recently as the mid-to-late Amazonian, we consider multiple localized geothermal events (separated in space and time) as the most likely explanation. Although volcano-tectonic activity in Tempe Terra is thought to have waned after the initial Hesperian graben forming phase (Hauber et al., 2010), our identification of a 1.0 ±

0.1 Ga lava flow in western Tempe Terra attests to Amazonian volcanic activity. If eruptive volcanism continued as recently as ~1 Ga, then subsequent non-eruptive geothermal heating events seem viable. A ~220 Ma magmato-tectonic phase could have enabled elevated geothermal heating and driven basal melting of VFFs and esker formation.

Modelling by Butcher et al. (2017) highlighted that strain heating could supplement geothermal heating in raising basal temperatures of VFFs to the melting point, and that convergent flow of ice in steep topographic settings could enhance this effect. The settings of the two VFFs associated with candidate eskers in western Tempe Terra are likely to have encouraged strain heating. For example, the parent VFF of System II terminates in a narrow valley which drained ice from a wider basin upslope, while System I originates at a significant break in topographic slope between the valley hosting the parent VFF and the flat surface of the *upper flow unit.*

With more sites of wet-based glaciation now identified in Tempe Terra, a regional climate warming event could provide a more straightforward explanation than spatially distributed geothermal heating, particularly if the three candidate eskers in western and northwestern Tempe Terra formed simultaneously. However, a general lack of evidence for surface (i.e., top-down) meltwater generation in the region (e.g., glacial meltwater channels) highlights the need for caution in invoking regional-scale climate warming as the sole driver of esker formation. Nonetheless, evidence for multiple sites of wet-based glaciation in Tempe Terra, combined with recent evidence for regionally-extensive wet-based glaciation in the Phlegra Montes region (Gallagher et al., 2021), suggests that there are significant gaps in our understanding of the thermal environment on Amazonian Mars, and its spatiotemporal complexities. Therefore, the involvement of climate change(s) and/or geothermal heating in inducing basal melting of viscous flow features on Mars requires further investigation.

7. Conclusions

We identify two sinuous ridges in western Tempe Terra, Mars, which we suggest are eskers. There is abundant evidence of Amazonian glaciation and deglaciation in the region and we document an assemblage of glacial landforms including viscous flow features (putative debris-covered glaciers), ice-cored moraines and the two candidate eskers. The candidate eskers emerge from 220 ± 40 Ma viscous flow features and overlie a 1.0 ± 0.1 Ga lava flow. After considering multiple formation hypotheses (including inverted paleochannels and volcanic features) and comparing the morphometries of the sinuous ridges to other Martian and terrestrial eskers, we interpret both sinuous ridges as glacial in origin and most likely eskers.

Our identification of two additional eskers in western Tempe Terra suggests that multiple Viscous Flow Features in this region produced meltwater in the past, at least transiently. The eskers extend from the same glaciated massif as the earlier-identified esker in northwest Tempe Terra (Butcher et al., 2017; Butcher et al., 2020), and lie ~600 km northwest of Chukhung crater (Butcher et al., 2021). As the two eskers in western Tempe Terra lie in grabens, this supports the previously proposed hypothesis that basal melting of viscous flow features was driven by locally elevated geothermal heating (Butcher et al., 2017; Gallagher and Balme, 2015). The spatial association of the eskers with an Amazonian-aged lava flow suggests that geothermal heating was a viable heat source for late-Amazonian wet-based glaciation. However, the newly-identified eskers also complicate this hypothesis, as geothermal heating would be required at multiple sites. Widespread regional geothermal heating would be uncharacteristic of the mid/late Amazonian epoch, so we suggest that multiple localized events would provide a more probable explanation. A surface heat source, such as regional climate warming, could provide an alternative explanation for multiple sites of wet-based glaciation; however, the lack of regional-scale evidence for surface meltwater production leads us to suggest

that basal heat sources (i.e., geothermal and strain heating) remain the best explanation for wet-based glaciation evidenced by eskers.

We highlight Tempe Terra as an area of interest for further wet-based glaciation studies, studies into Mars' recent palaeo-environment, and a site for future exploration. Our identification of two additional eskers in Tempe Terra contributes to a better characterization of the recent glacial history of the region and highlights that further paleo-environmental investigations are required to better understand the thermal environment of the region (and its spatiotemporal variations) during the Amazonian period. We also contribute morphometric measurements for the candidate eskers in western Tempe Terra, which can aid future investigations into the origin of esker-like sinuous ridges elsewhere on Mars.

Declaration of Competing Interest

None.

Acknowledgements

Appendix A. Supplementary data

Supplementary data to this article can be found online at https://doi.org/10.1016/j.icarus.2022.115147.

References

Allen, C.C., 1979. Volcano-ice interactions on Mars. J. Geophys. Res. 84 (B14), 8048–8059. https://doi.org/10.1029/JB084iB14p08048.

Baker, D.M., Head, J.W., 2015. Extensive middle Amazonian mantling of debris aprons and plains in Deuteronilus Mensae, Mars: implications for the record of mid-latitude glaciation. Icarus 260, 269–288. https://doi.org/10.1016/j.icarus.2015.06.036.

Banks, M.E., Lang, N.P., Kargel, J.S., McEwen, A.S., Baker, V.R., Grant, J.A., Pelletier, J.D., Strom, R.G., 2009. An analysis of sinuous ridges in the southern Argyre Planitia, Mars using HiRISE and CTX images and MOLA data. J. Geophys. Res. 114 (E09) https://doi.org/10.1029/2008JE003244.

Benn, D., Evans, D.J., 2010. Glaciers and Glaciation, Second edition. Routledge, New York. ISBN 13: 978-0-340-90579-1.

Bernhardt, H., Hiesinger, H., Reiss, D., Ivanov, M., Erkeling, G., 2013. Putative eskers and new insights into glacio-fluvial depositional settings in southern Argyre Planitia, Mars. P&SS 85, 261–278. https://doi.org/10.1016/j.pss.2013.06.022.

Bouley, S., Baratoux, D., Paulien, N., Missenard, Y., Saint-Bezar, B., 2018. The revised tectonic history of Tharsis. Earth Planet. Sci. Lett. 488, 126–133. https://doi.org/10.1016/j.epsl.2018.02.019.

Brennand, T.A., 2000. Deglacial meltwater drainage and glaciodynamics: inferences from Laurentide eskers, Canada. Geomorphology 32 (3–4), 263–293. https://doi.org/10.1016/S0169-555X(99)00100-2.

Brož, P., Krýza, O., Lionel Wilson, L., Conway, S.J., Hauber, E., Mazzini, A., Jan Raack, J., Balm, M.R., Sylvestand, M.E., Patel, M.R., 2020a. Experimental evidence for lava-like mud flows under Martian surface conditions. Nat. Geosci. 13 (6), 403–407. https://doi.org/10.1038/s41561-020-0577-2.

Brož, P., Krýza, O., Conway, S.J., Mueller, N.T., Hauber, E., Mazzini, A., Raack, J., Balme, M.R., Sylvest, M.E., Patel, M.R., 2020b. Mud flow levitation on Mars: insights from laboratory simulations. Earth Planet. Sci. Lett. 545, 116406 https://doi.org/10.1016/j.epsl.2020.116406.

Burke, M.J., Woodward, J., Russell, A.J., Fleisher, P.J., Bailey, P.K., 2008. Controls on the sedimentary architecture of a single event englacial esker: Skeiðarárjökull, Iceland. Quat. Sci. Rev. 27 (19–20), 1829–1847. https://doi.org/10.1016/j.quascirev.2008.06.012.

Burke, M.J., Brennand, T.A., Perkins, A.J., 2012. Transient subglacial hydrology of a thin ice sheet: insights from the chasm esker, British Columbia, Canada. Quat. Sci. Rev. 58, 30–55. https://doi.org/10.1016/j.quascirev.2012.09.004.

Burr, D.M., Enga, M.T., Williams, R.M.E., Zimbelman, J.R., Howard, A.D., Brennand, T. A., 2009. Pervasive aqueous paleoflow features in the Aeolis/Zephyria Plana region, Mars. Icarus 200, 52–76. https://doi.org/10.1016/j.icarus.2008.10.014.

Butcher, F.E.G., 2019. Wet-Based Glaciation on Mars (PhD Thesis). The Open University, Milton Keynes, UK. http://oro.open.ac.uk/id/eprint/60703.

Butcher, F.E.G., Conway, S.J., Arnold, N.S., 2016. Are the Dorsa Argentea on Mars eskers? Icarus 275, 65–84. https://doi.org/10.1016/j.icarus.2016.03.028.

Butcher, F.E.G., Balme, M.R., Gallagher, C., Arnold, N.S., Conway, S.J., Hagermann, A., Lewis, S.R., 2017. Recent basal melting of a mid-latitude glacier on Mars. J. Geophys. Res. Planets 122, 2445–2468. https://doi.org/10.1002/2017JE005434.

Butcher, F.E.G., Balme, M.R., Conway, S.J., Gallagher, C., Arnold, N.S., Storrar, R.D., Lewis, S.R., Hagermann, A., 2020. Morphometry of a glacier-linked esker in NW Tempe Terra, Mars, and implications for sediment-discharge dynamics of subglacial drainage. Earth Planet. Sci. Lett. 542, 116325 https://doi.org/10.1016/j.epsl.2020.116325.

Butcher, F.E.G., Balme, M.R., Conway, S.J., Gallagher, C., Arnold, N.S., Storrar, R.D., Lewis, S.R., Hagermann, A., Davis, J.M., 2021. Sinuous ridges in Chukhung Crater, Tempe Terra, Mars: implications for fluvial, glacial, and glaciofluvial activity. Icarus 357, 114131. https://doi.org/10.1016/j.icarus.2020.114131.

Carr, M.H., Head, J.W., 2010. Geologic history of Mars. Earth Planet. Sci. Lett. 294, 185–203. https://doi.org/10.1016/j.epsl.2009.06.042.

Crown, D.A., Ramsay, M.S., 2016. Morphologic and thermophysical characteristics of lava flows southwest of Arsia Mons, Mars. J. Volcanol. Geotherm. Res. 342, 13–28. https://doi.org/10.1016/j.jvolgeores.2016.07.008.

Deardorff, N., Booth, A., Cashman, K., 2019. Remote characterization of dominant wavelengths from surface folding on lava flows using lidar and discrete Fourier transform analyses. Geochem. Geophys. 20 (8), 3952–3970. https://doi.org/10.1029/2019GC008497.

Doelling, H.H., 2002. Interim geologic map of the San Rafael Desert 30′ x 60′ quadrangle, Emery and Grand Counties, Utah Geological Survey Open-File Report 404, scale 1: 100,000.

Gallagher, C., Balme, M., 2015. Eskers in a complete, wet-based glacial system in the Phlegra Montes region. Mars. Earth Planet. Sci. Lett. 431, 96–109. https://doi.org/10.1016/j.epsl.2015.09.023.

Gallagher, C., Butcher, F.E., Balme, M., Smith, I., Arnold, N., 2021. Landforms indicative of regional warm based glaciation, Phlegra Montes. Mars. Icarus 355, 114173. https://doi.org/10.1016/j.icarus.2020.114173.

Gorrell, G., Shaw, J., 1991. Deposition in an esker, bead and fan complex, Lanark, Ontario, Canada. Sediment. Geol. 72 (3–4), 285–314. https://doi.org/10.1016/0037-0738(91)90016-7.

Gregg, T.K.P., Fink, J.H., Griffioth, R.W., 1998. Formation of multiple fold generations on lava flow surfaces: influence of strain rate, cooling rate, and lava composition. J. Volcanol. Geotherm. Res. 80, 281–292. https://doi.org/10.1016/S0377-0273(97)00048-6.

Hartmann, W.K., 2005. Martian cratering 8: Isochron refinement and the chronology of Mars. Icarus 174, 294–320. https://doi.org/10.1016/j.icarus.2004.11.023.

Hartmann, W.K., Neukum, G., 2001. Cratering Chronology and the Evolution of Mars. Chronology and Evolution of Mars. Space Sciences Series of ISSI 12, 165–194. https://doi.org/10.1007/978-94- 017-1035-0_6.

Hauber, E., Grott, M., Kronberg, P., 2010. Martian rifts: structural geology and geophysics. Earth Planet. Sci. Lett. 294, 393–410. https://doi.org/10.1016/j.epsl.2009.11.005.

Head, J.W., Mustard, J.F., Kreslavsky, M.A., Milliken, R.E., Marchant, D.R., 2003. Recent ice ages on Mars. Nature 426 (6968), 797–802. https://doi.org/10.1038/nature02114.

Head, J.W., Marchant, D.R., Dickson, J.L., Kress, A.M., Baker, D.M., 2010. Northern mid-latitude glaciation in the late Amazonian period of Mars: criteria for the recognition of debris-covered glacier and valley glacier landsystem deposits. Earth Planet. Sci. Lett. 294, 306–320. https://doi.org/10.1016/j.epsl.2009.06.041.

Hepburn, A.J., Ng, F.S.L., Holt, T.O., Hubbard, B., 2020. Late Amazonian Ice Survival in Kasei Valles. Mars. J. Geophys. Res. 125 (11), e2020JE006531 https://doi.org/10.1029/2020JE006531.

Holt, J.W., Safaeinili, A., Plaut, J.J., Head, J.W., Phillips, R.J., Seu, R., Kempf, S.D., Choudhary, P., Young, D.A., Putzig, N.E., Biccari, D., Gim, Y., 2008. Radar sounding evidence for buried glaciers in the southern mid-latitudes of Mars. Science 322, 1235–1238. https://doi.org/10.1126/science.1164246.

Hungerford, J.D.G., Edwards, B.R., Skilling, I.P., Cameron, B.I., 2014. Evolution of a subglacial basaltic lava flow field: Tennena volcanic center, Mount Edziza volcanic complex, British Columbia, Canada. J. Volcanol. Geotherm. Res. 272, 39–58. https://doi.org/10.1016/j.jvolgeores.2013.09.012.

Ingólfsson, Ó., Benediktsson, Í.Ö., Schomacker, A., Kjær, K.H., Brynjólfsson, S., Jónsson, S.A., Johnson, M.D., 2016. Glacial geological studies of surge-type glaciers in Iceland—research status and future challenges. Earth Sci. Rev. 152, 37–69. https://doi.org/10.1016/j.earscirev.2015.11.008.

Ivanov, B.A., 2001. Mars/Moon cratering rate ratio estimates. Space Sci. Rev. 96, 87–104. https://doi.org/10.1023/A:1011941121102.

Kirk, R.L., Howington-Kraus, E., Rosiek, M.R., Anderson, J.A., Archinal, B.A., Becker, K. J., Cook, D.A., Galuszka, D.M., Geissler, P.E., Hare, T.M., Holmberg, I.M., Keszthelyi, L.P., Redding, B.L., Delamere, W.A., Gallagher, D., Chapel, J.D., Eliason, E.M., King, R., McEwen, A.S., Holmberg, I.M., 2008. Ultrahigh resolution topographic mapping of Mars with MRO HiRISE stereo images: meter-scale slopes of candidate Phoenix landing sites. J. Geophys. Res. 113 (E3) https://doi.org/10.1029/2007JE003000.

Kneissl, T., van Gasselt, S., Neukum, G., 2011. Map-projection-independent crater size-frequency determination in GIS environments—new software tool for ArcGIS. Planet. Space Sci. 59, 1243–1254. https://doi.org/10.1016/j.pss.2010.03.015.

Laskar, J., Correia, A.C.M., Gastineau, M., Joutel, F., Levrard, B., Robutel, P., 2004. Long term evolution and chaotic diffusion of the insolation quantities of Mars. Icarus 170 (2), 343–364. https://doi.org/10.1016/j.icarus.2004.04.005.

Lasue, J., Mangold, N., Hauber, E., Clifford, S., Feldman, W., Gasnault, O., Grima, C., Maurice, S., Mousis, O., 2013. Quantitative assessments of the martian hydrosphere. Space Sci. Rev. 174 (1–4), 155–212. https://doi.org/10.1007/s11214-012-9946-5.

Levy, J.S., Marchant, D.R., Head, J.W., 2010a. Thermal contraction crack polygons on Mars: a synthesis from HiRISE, Phoenix, and terrestrial analog studies. Icarus 206 (1), 229–252. https://doi.org/10.1016/j.icarus.2009.09.005.

Levy, J., Head, J.W., Marchant, D.R., 2010b. Concentric crater fill in the northern mid-latitudes of Mars: formation processes and relationships to similar landforms of glacial origin. Icarus 209 (2), 390–404. https://doi.org/10.1016/j.icarus.2010.03.036.

Livingstone, S.J., Lewington, E.L., Clark, C.D., Storrar, R.D., Sole, A.J., McMartin, I., Dewald, N., Ng, F., 2020. A quasi-annual record of time-transgressive esker formation: implications for ice-sheet reconstruction and subglacial hydrology. Cryosphere 14 (6), 1989–2004. https://doi.org/10.5194/tc-14-1989-2020.

Mäkinen, J., 2003. Time-transgressive deposits of repeated depositional sequences within interlobate glaciofluvial (esker) sediments in Köyliö, SW Finland. Sedimentology 50 (2), 327–360. https://doi.org/10.1046/j.1365-3091.2003.00557.x.

Malin, M.C., Edgett, K.S., 2003. Evidence for persistent flow and aqueous sedimentation on early Mars. Science 302 (5652), 1931–1934. https://doi.org/10.1126/science.1090544.

Malin, M.C., Bell, J.F., Cantor, B.A., Caplinger, M.A., Calvin, W.M., Clancy, R.T., Edgett, K.S., Edwards, L., Haberle, R.M., James, P.B., Lee, S.W., Ravine, M.A., Thomas, P.C., Wolff, M.J., 2007. Context camera investigation on board the Mars Reconnaissance Orbiter. J. Geophys. Res. 112, E05S04. https://doi.org/10.1029/2006JE002808.

McEwen, A.S., Eliason, E.M., Bergstrom, J.W., Bridges, N.T., Hansen, C.J., Delamere, W.A., Grant, J.A., Gulick, V.C., Herkenhoff, K.E., Keszthelyi, L., Kirk, R.L., Mellon, M.T., Squyres, S.W., Thomas, N., Weitz, C.M., 2007. Mars Reconnaissance Orbiter's high resolution imaging science experiment (HiRISE). J. Geophys. Res. 112, E05S02. https://doi.org/10.1029/2005JE002605.

Michael, G.G., Neukum, G., 2010. Planetary surface dating from crater size-frequency distribution measurements: partial resurfacing events and statistical age uncertainty. EPSL. 294 (3–4), 223–229. https://doi.org/10.1016/j.epsl.2009.12.041.

Milliken, R.E., Mustard, J.F., Goldsby, D.L., 2003. Viscous flow features on the surface of Mars: observations from high-resolution Mars Orbiter Camera (MOC) images. J. Geophys. Res. 108 (E6) https://doi.org/10.1029/2002JE002005.

Mustard, J.F., Cooper, C.D., Rifkin, M.K., 2001. Evidence for recent climate change on Mars from the identification of youthful near-surface ground ice. Nature 412, 411–414. https://doi.org/10.1038/35086515.

Neukum, G., Jaumann, R., The HRSC Co-Investigator and Experiment Team, 2004. HRSC: the high resolution stereo camera of Mars Express. In: Wilson, A. (Ed.), Mars Express: The Scientific Payload, 1240. European Space Agency Special Publication, pp. 17–35. ISBN 92-9092-556-6.

Pain, C.F., Oilier, C.D., 1995. Inversion of relief — a component of landscape evolution. Geomorphology 12, 151–165. https://doi.org/10.1016/0169-555X(94)00084-5.

Pedersen, G.B.M., 2013. Frozen Martian lahars? Evaluation of morphology, degradation and geologic development in the Utopia–Elysium transition zone. P&SS 85, 59–77. https://doi.org/10.1016/j.pss.2013.05.020.

Petersen, E.I., Holt, J.W., Levy, J.S., 2018. High ice purity of Martian lobate debris aprons at the regional scale: evidence from an orbital radar sounding survey in Deuteronilus and Protonilus Mensae. Geophys. Res. Lett. 45, 11,595–11,604. https://doi.org/10.1029/2018GL079759.

Pierce, T.L., Crown, D.A., 2003. Morphologic and topographic analyses of debris aprons in the eastern Hellas region. Mars. Icarus 163 (1), 46–65. https://doi.org/10.1016/S0019-1035(03)00046-0.

Richardson, J.A., Bleacher, J.E., Connor, C.B., Glaze, L.S., 2021. Small volcanic vents of the Tharsis Volcanic Province, Mars. J. Geophys. Res. Planets 126 (2). https://doi.org/10.1029/2020JE006620.

Schon, S.C., Head, J.W., Milliken, R.E., 2009. A recent ice age on Mars: evidence for climate oscillations from regional layering in mid-latitude mantling deposits. Geophys. Res. Lett. 36 (15) https://doi.org/10.1029/2009GL038554.

Shreve, R.L., 1985. Esker characteristics in terms of glacier physics, Katahdin esker system, Maine. Geol. Soc. Am. Bull. 96, 639–646. https://doi.org/10.1130/0016-7606(1985)96<639:ECITOG>2.0.CO;2.

Squyres, S.W., 1979. The distribution of lobate debris aprons and similar flows on Mars. J. Geophys. Res. 84, 8087–8096. https://doi.org/10.1029/JB084iB14p08087.

Squyres, S.W., Clifford, S.M., Kuzmin, R.O., Zimbelman, J.R., Costard, F., 1992. Ice in the Martian Megaregolith. Mars, Chapter 16, pp. 523–560. ISBN 0-8165-1257-4.

Storrar, R.D., Stokes, C.R., Evans, D.J., 2013. A map of large Canadian eskers from Landsat satellite imagery. J. Maps 9 (3), 456–473. https://doi.org/10.1080/17445647.2013.815591.

Storrar, R.D., Stokes, C.R., Evans, D.J.A., 2014. Morphometry and pattern of a large sample (>20,000) of Canadian eskers and implications for subglacial drainage beneath ice sheets. Quat. Sci. Rev. 105, 1–25. https://doi.org/10.1016/j.quascirev.2014.09.013.

Storrar, R.D., Evans, D.J., Stokes, C.R., Ewertowski, M., 2015. Controls on the location, morphology and evolution of complex esker systems at decadal timescales, Breiðamerkurjökull, Southeast Iceland. Earth Surf. Process. Landf. 40 (11), 1421–1438. https://doi.org/10.1002/esp.3725.

Tanaka, K.L., Skinner, J.A., Dohm, J.M., Irwin III, R.P., Kolb, E.J., Fortezzo, C.M., Platz, T., Michael, G.G., Hare, T., 2014a. Geologic Map of Mars, US Geologic Survey Scientific Investigations Map 3292, scale 1:20,000,000, with 43 p. pamphlet.

Tanaka, K.L., Skinner, J.A., Dohm, J.M., Irwin III, R.P., Kolb, E.J., Fortezzo, C.M., Platz, T., Michael, G.G., Hare, T., 2014b. Geologic Map of Mars, Pamphlet to Accompany Scientific Investigations Map 3292. US Geological Survey.

Van Gasselt, S., Hauber, E., Rossi, A.P., Dumke, A., Orosei, R., Neukum, G., 2011. Periglacial geomorphology and landscape evolution of the Tempe Terra region, Mars. Geol. Soc. Lond., Spec. Publ. 356 (1), 43–67.

Warner, N.H., Gupta, S., Calef, F., Grindrod, P., Boll, N., Goddard, K., 2015. Minimum effective area for high resolution crater counting of martian terrains. Icarus 245, 198–240. https://doi.org/10.1016/j.icarus.2014.09.024.

Wilson, L., Mouginis-Mark, P.J., 2014. Dynamics of a fluid flow on Mars: lava or mud? Icarus 233, 268–280. https://doi.org/10.1016/j.icarus.2014.01.041.